AIP | Physics of Fluids

Pure and aerated water entry of a flat plate

Z. H. Ma, D. M. Causon, L. Qian, C. G. Mingham, T. Mai, D. Greaves, and A. Raby

Citation: Physics of Fluids **28**, 016104 (2016); doi: 10.1063/1.4940043
View online: http://dx.doi.org/10.1063/1.4940043
View Table of Contents: http://scitation.aip.org/content/aip/journal/pof2/28/1?ver=pdfcov
Published by the AIP Publishing

Articles you may be interested in

On shock driven jetting of liquid from non-sinusoidal surfaces into a vacuum
J. Appl. Phys. **118**, 185901 (2015); 10.1063/1.4934645

Measurement and discrete element simulation of a fixed-obstacle disturbed rapid granular chute flow
Phys. Fluids **27**, 013305 (2015); 10.1063/1.4906769

Flows around a cascade of flat plates with acoustic resonance
Phys. Fluids **25**, 106104 (2013); 10.1063/1.4825376

An experimental research on the flow field of water entry by pressure measurements
Phys. Fluids **13**, 347 (2001); 10.1063/1.1329907

An experimental study of density waves in a hypersonic shock layer on a flat plate
Phys. Fluids **12**, 1544 (2000); 10.1063/1.870403

This article is copyrighted as indicated in the article. Reuse of AIP content is subject to the terms at: http://scitation.aip.org/termsconditions. Downloaded to IP: 149.170.118.205 On: Tue, 26 Jan 2016 09:29:20

PHYSICS OF FLUIDS **28**, 016104 (2016)

Pure and aerated water entry of a flat plate

Z. H. Ma,[1,a)] D. M. Causon,[1] L. Qian,[1] C. G. Mingham,[1] T. Mai,[2] D. Greaves,[2] and A. Raby[2]
[1]*School of Computing, Mathematics and Digital Technology, Manchester Metropolitan University, Manchester M1 5GD, United Kingdom*
[2]*School of Marine Science and Engineering, Plymouth University, Plymouth PL4 8AA, United Kingdom*

(Received 3 August 2015; accepted 4 January 2016; published online 25 January 2016)

This paper presents an experimental and numerical investigation of the entry of a rigid square flat plate into pure and aerated water. Attention is focused on the measurement and calculation of the slamming loads on the plate. The experimental study was carried out in the ocean basin at Plymouth University's COAST laboratory. The present numerical approach extends a two-dimensional hydro-code to compute three-dimensional hydrodynamic impact problems. The impact loads on the structure computed by the numerical model compare well with laboratory measurements. It is revealed that the impact loading consists of distinctive features including (1) shock loading with a high pressure peak, (2) fluid expansion loading associated with very low sub-atmospheric pressure close to the saturated vapour pressure, and (3) less severe secondary reloading with super-atmospheric pressure. It is also disclosed that aeration introduced into water can effectively reduce local pressures and total forces on the flat plate. The peak impact loading on the plate can be reduced by half or even more with 1.6% aeration in water. At the same time, the lifespan of shock loading is prolonged by aeration, and the variation of impulse is less sensitive to the change of aeration than the peak loading. © *2016 Author(s). All article content, except where otherwise noted, is licensed under a Creative Commons Attribution (CC BY) license (http://creativecommons.org/licenses/by/4.0/).* [http://dx.doi.org/10.1063/1.4940043]

I. INTRODUCTION

Hydrodynamic impact problems are frequently encountered in natural hazards,[1,2] marine engineering,[3–5] and water sports.[6] Under violent wave conditions, the bow of a ship can emerge from the water then re-enter water with high speed. This may cause severe local damage and high-frequency global stresses in the structure.[7] In certain emergency situations, civil or military aircraft need to ditch on the water to evacuate the crew and passengers. Impulsive slamming pressures and forces exerted on the fuselage will potentially damage the aircraft and threaten lives.[8] In competitive diving, especially the 10 m platform diving of the Olympic Games or world championships, athletes need to repeatedly impinge on the water surface with relatively high speed near or over 14 m/s. This leads to strong impact loads on the human body. Long-term such intensive practice will very likely cause severe injuries to limbs, shoulder, spine, retina, and other organs of the athletes.[6,9,10] Therefore, the accurate prediction of slamming loads on solid structures and human bodies is of great importance to further scientific research and engineering applications.

Early investigation of the slamming loads on solid structures can be traced back to the pioneering work of von Karman for the aircraft ditching problem.[11] For a flat-bottomed float, he proposed that the peak pressure $p_{\max}$ is related to the water density ρ, speed of sound in water c, and impact velocity v as $p_{\max} = \rho c v$. This is usually referred as the acoustic pressure. In the following several decades, different theories for predicting hydrodynamic impact loads were proposed by other

[a)]Author to whom correspondence should be addressed. Electronic mail: z.ma@mmu.ac.uk

 © Author(s) 2016.

This article is copyrighted as indicated in the article. Reuse of AIP content is subject to the terms at: http://scitation.aip.org/termsconditions. Downloaded to IP: 149.170.118.205 On: Tue, 26 Jan 2016 09:29:20

researchers including Pabst,[12] Wagner,[13] Korobkin and Pukhnachov,[14] Howison *et al.*,[15] and references therein. Some researchers also paid attention to other problems pertaining to the slamming of plates, e.g., added masses of thin rectangular plates in nonlifting potential flow.[16]

On the other hand, researchers have carried out experiments to study the impact pressures on flat-bottom structures and observed that their measurements were below the acoustic pressure proposed by von Karman.[17–19] Careful inspections reveal that the underlying reason causing this discrepancy is the cushioning effect of the air layer trapped by the flat plate.[20,21] This was ignored in the acoustic pressure formula of von Karman.[11] For other blunt bodies like cylinders or hemispheres, recent experiments show that air is entrained into the water during the slamming event.[22–24]

During water entry, flat plates and other blunt bodies usually trap air beneath their lower rigid or flexible surface. The air is extensively compressed and forms a very thin layer as the structure approaches the water surface. It may also expand afterwards when the pressure drops. The trapped air layer may repeat the expansion and contraction cycle leading to pulsating loads on the structure.

The problem becomes even more complicated when air bubbles are present in the water. In the ocean, bubbles are entrained/generated in the water by a number of different processes including biological production, entrapment of air by capillary waves, white capping, and wave breaking.[25] These bubbles generally persist for many wave periods in seawater and do not tend to coalesce and hence remain small, rising slowly through the water.[26] For wave breaking on structures, aeration has an effect on the impact loading causing discrepancies in time histories and maximum values of pressure between pure fresh water and aerated fresh water.[27–29] Despite these past crucial research works, studies of the bubble effect during the entry of flat plates or other blunt bodies into aerated water are quite limited so far.

To the knowledge of the authors, quantitative numerical and experimental studies of the impact loads on a flat plate during entry into pure and aerated water have not been reported in the literature. The lack of such reported studies is due to the significant challenges presented to both numerical methods and laboratory setup and measurement techniques.

Although numerical methods based on the potential flow model or incompressible single-/two-phase Navier–Stokes equations have been more frequently used in hydrodynamics, the complex phenomena of compression, expansion, and ventilation of fluid[4] occurring in violent slamming events, particularly, in the case of aerated conditions cannot directly be handled by the aforementioned methods. This requires a more detailed compressible multiphase flow model that can include all necessary physics to provide an accurate solution.[5] Moreover, it demands the numerical model's capability properly to handle the air-bubble/water mixture, of which the acoustic property is significantly different with pure water as shown in Figure 1. This figure illustrates the speed of sound in a water-air mixture.[30] It is clearly observed that introducing 1% volume fraction of air into the water reduces the sound speed from around 1500 m/s to less than 200 m/s. Some researchers also stated that incipient flow cavitation, during which the water undergoes a phase change to form vapour bubbles when the pressure reduces towards the limit of saturated vapour pressure, may occur in

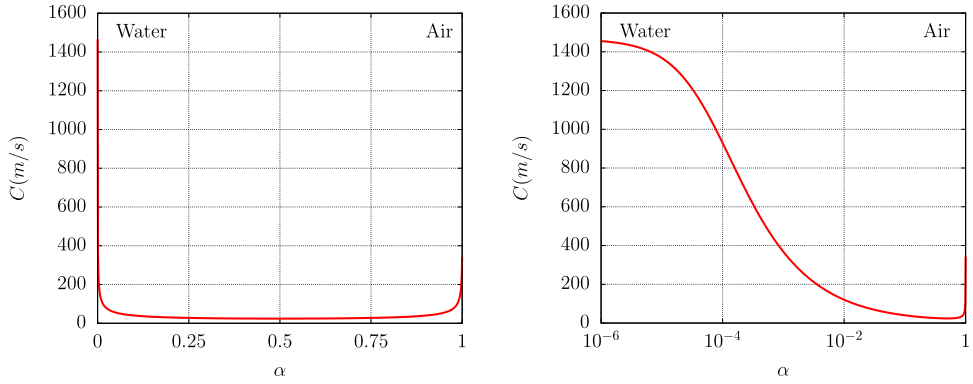

FIG. 1. The speed of sound in water-air mixture at one atmospheric pressure and 15 °C.[30] α indicates the volume fraction of air in the mixture. Left: normal scale; right: log scale.

This article is copyrighted as indicated in the article. Reuse of AIP content is subject to the terms at: http://scitation.aip.org/termsconditions. Downloaded to IP: 149.170.118.205 On: Tue, 26 Jan 2016 09:29:20

hydrodynamic slamming events.[4,8] Numerical methods may easily fail to handle the low pressure associated with cavitation and to capture the subsequent re-loading on the structure.

On the other hand, in the laboratory, due to the intensity of the high speed slamming event, experimental studies of a flat-bottom object slamming into water with an impact velocity of over 5 m/s are quite rare. Meanwhile, most of the reported experiments focus attention upon pure water entry without considering aerated water.

In the present work, we make an effort to carry out an experimental and numerical study of pure and aerated water entry of a square rigid flat plate. We focus here on the measurement and calculation of the slamming loads on the plate with a vertical impact velocity over 5 m/s. The experimental study was carried out in the ocean basin at Plymouth University's COAST laboratory, without the wave paddles in operation. The fresh water was artificially aerated by pumping bubbles into it through a perforated plastic plate placed at the bottom of the basin.[31] A novel in-house two-dimensional hydro-code[32] is extended here to compute three-dimensional hydrodynamic impact problems. The numerical model has the capability to deal with trapped air layer and a water-air mixture in both high and low pressure regions fully accounting for compressibility and cavitation effects.

The shape of our test object, a square flat plate with no curvature, may appear to be simple but it is closely related to real applications, e.g., (1) the hull of large ships like floating production storage and offloading units (FPSOs) usually has a large area of flat surface; (2) divers often use a flat-hand entry technique (or accidentally use back entry), the hands are brought together with palms facing the water in order to accomplish a splash-less entry. Therefore, it is very important to investigate the water entry of flat-bottom structures.

The remainder of the paper is organised as follows: The experimental setup for the flat plate slamming problem is first described in Section II. Summary details of the numerical model are provided in Section III, and further details can be found in the work of Ma *et al.*[32] The numerical results and laboratory measurements for pure and aerated water entries are presented in Section IV. Finally, some conclusions are drawn and future work is discussed in Section V.

II. EXPERIMENT SETUP

The experimental study was carried out in the ocean basin at Plymouth University's COAST Laboratory. The ocean basin is 35 m long by 15.5 m wide and has an adjustable floor allowing operation at different water depths up to 3 m.

A. Test object

The falling block includes a rigid flat impact plate connected to two driver plates and its total mass can be varied from 32 kg (block 1) to 52 kg (block 2). The impact plate is 0.25 m long and 0.25 m wide with a thickness of 0.012 m. The impact velocity can vary between 4 m/s and 7 m/s by adjusting the initial position of the plate. Pressures were measured during impact by five miniature pressure transducers (Model XPM10) installed on the impact plate as illustrated in Figure 2. The actual impact velocity was integrated from the measured data recorded by an accelerometer (Model 4610) mounted on the top of the flat plate. Both pressure and acceleration data were sampled at a frequency of 50 kHz. In the experiment, the force is obtained by integrating the pressures gauged at five locations with the following formula:

$$F = \sum_{i=1}^{5} p_i S_i \tag{1}$$

in which p_1–p_5 are the pressures; S_1–S_5 are the influence areas set as $S_1 = 0.0121\ \mathrm{m}^2$ and $S_2 = S_3 = S_4 = S_5 = 0.0126\ \mathrm{m}^2$.

B. Air bubble generation

The water was aerated by introducing air bubbles into it. The void fraction (or aeration level) of the aerated water can be controlled by the air compressor by adjusting the injection pressure into

This article is copyrighted as indicated in the article. Reuse of AIP content is subject to the terms at: http://scitation.aip.org/termsconditions. Downloaded to IP: 149.170.118.205 On: Tue, 26 Jan 2016 09:29:20

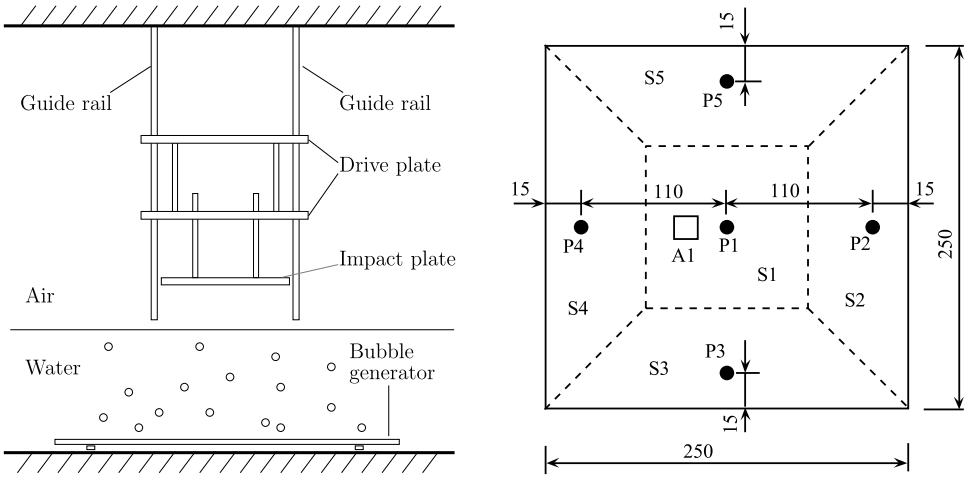

FIG. 2. Experiment setup. Left: a sketch of the facility; right: configuration of the instrumentation on the impact plate. (Units in mm.) P1–P5 are pressure transducers, S1–S5 are the influence areas of the pressure transducers, and A1 is the accelerometer.

the bubble generator. The generator was made of clear plastic with six flat surfaces including the top, bottom, and four sides. Each of the four side surfaces has an air inlet, through which the compressed air was injected into the generator as shown in Figure 3. The top surface, of which the dimensions are $0.54 \times 0.54 \times 0.002$ m, is perforated by an array of circular holes drilled by a laser cutter. The holes are distributed over a square area of 0.495×0.495 m^2. The spacing between each of neighbouring holes is 1 cm and the diameter of each hole is around 0.2 mm. The bubble generator was placed at the bottom of ocean basin with water depth of 1 m. Snapshots of the aerated water generated by different injection pressures are illustrated in Figure 4, which clearly shows that the bubble density increases with injection pressure.

C. Void fraction estimations

There are several applicable methodologies for determining the void fraction of aerated water including measurement of the speed of sound, a volumetric method, hydrostatic pressure in aerated water, and high speed photography to estimate bubble size, distribution, and velocity. Each of these methods has its own advantages and difficulties.[31]

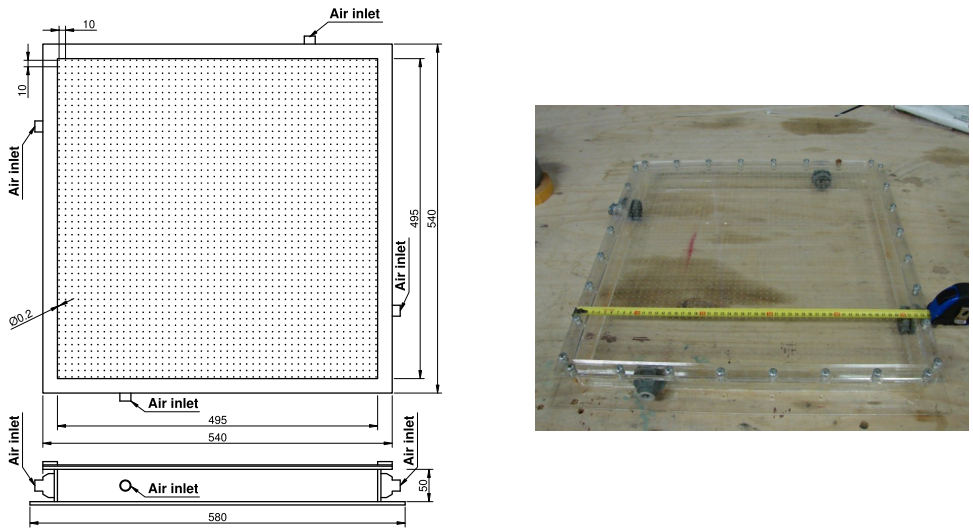

FIG. 3. The bubble generator (units in mm).

This article is copyrighted as indicated in the article. Reuse of AIP content is subject to the terms at: http://scitation.aip.org/termsconditions. Downloaded to IP: 149.170.118.205 On: Tue, 26 Jan 2016 09:29:20

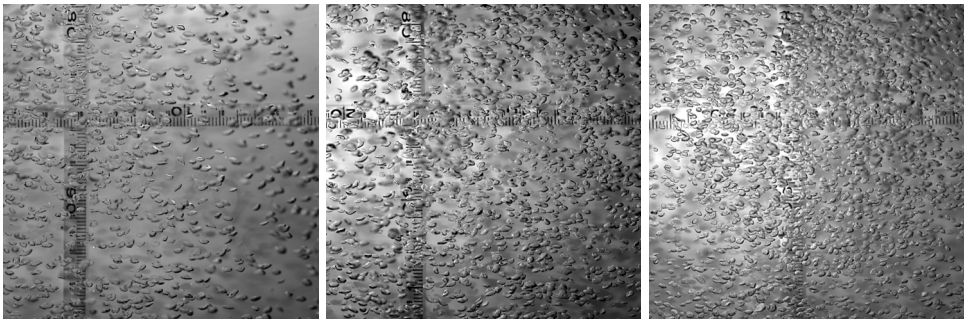

(a) (b) (c)

FIG. 4. Aerated water generated at different air injection pressures. (a) 0.065 bars. (b) 0.083 bars. (c) 0.137 bars.

In the present work, the volumetric method (air flow rate measurement) was used to estimate the void fraction in the ocean basin by using the following formula:

$$\alpha = \left(1 + \frac{1}{2\kappa}\frac{\Delta p}{p_{\mathrm{a}}}\right)\frac{t_{\mathrm{r}}}{t_{\mathrm{f}}}, \tag{2}$$

where κ is the adiabatic coefficient, Δp is the change in pressure given by the weight of the water column, p_{a} is the atmospheric pressure, t_{r} is the time a bubble needs to reach surface after leaving the bubble generator, and t_{f} is the time needed to completely fill the cylinder with air. A clear plastic cylinder was used to measure the air flow rate through the water body as shown in Figures 5(a) and 5(b). The air flow rate of each aeration level was measured at nine spatial locations indicated in Figure 5(c). The void fractions calibrated by the flow rate method in the ocean basin are presented in Figure 6. The calibration was carried out at a depth of 25 cm from the water surface.

III. NUMERICAL MODEL

The mathematical model used here for the flow of the compressible air and water/air-bubble mixture consists of the mass, momentum, and energy conservation laws for the fluid. A conservation law of mass for each phase is also included. A non-conservative equation for the advection of gas-phase volume fraction function also needs to be included. Though inertia usually plays a much more dominant role in hydrodynamic impact problems compared to gravity, the gravitational terms

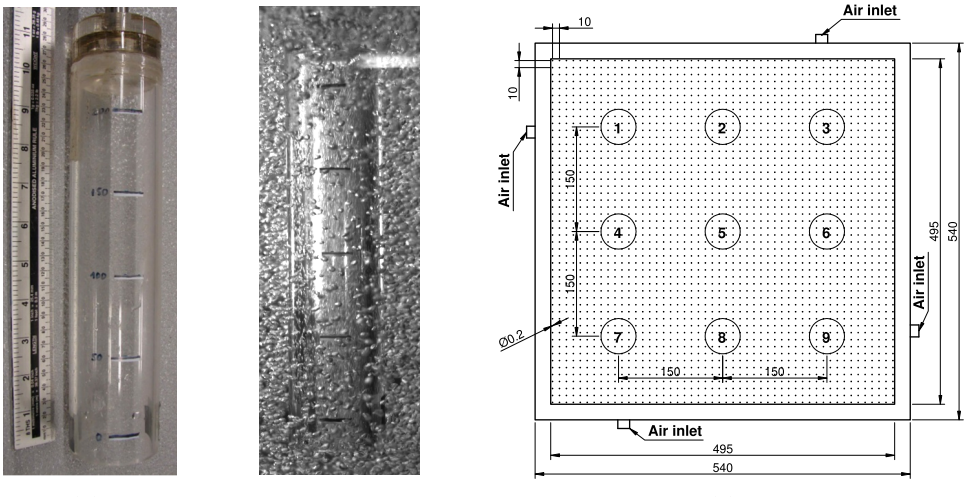

(a) (b) (c)

FIG. 5. The clear plastic cylinder and the measured locations.

This article is copyrighted as indicated in the article. Reuse of AIP content is subject to the terms at: http://scitation.aip.org/termsconditions. Downloaded to IP: 149.170.118.205 On: Tue, 26 Jan 2016 09:29:20

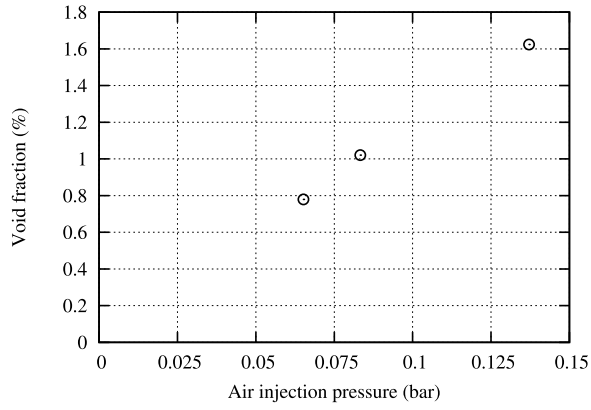

FIG. 6. Void fraction calibrated in the ocean basin.

remain included in the flow model. The whole system can be expressed as

$$\frac{\partial}{\partial t}\begin{bmatrix}\alpha_1\rho_1\\ \alpha_2\rho_2\\ \rho u\\ \rho v\\ \rho w\\ \rho E\end{bmatrix}+\frac{\partial}{\partial x}\begin{bmatrix}\alpha_1\rho_1 u\\ \alpha_2\rho_2 u\\ \rho u^2+p\\ \rho v u\\ \rho w u\\ \rho h u\end{bmatrix}+\frac{\partial}{\partial y}\begin{bmatrix}\alpha_1\rho_1 v\\ \alpha_2\rho_2 v\\ \rho u v\\ \rho v^2+p\\ \rho w v\\ \rho h v\end{bmatrix}+\frac{\partial}{\partial z}\begin{bmatrix}\alpha_1\rho_1 w\\ \alpha_2\rho_2 w\\ \rho u w\\ \rho v w\\ \rho w^2+p\\ \rho h w\end{bmatrix}=\begin{bmatrix}0\\ 0\\ 0\\ -\rho g\\ 0\\ -\rho g v\end{bmatrix}, \tag{3a}$$

$$\frac{\partial\alpha_1}{\partial t}+\vec{V}\cdot\nabla\alpha_1=K\nabla\cdot\vec{V}, \tag{3b}$$

where α_1 and α_2 satisfying $\alpha_1+\alpha_2=1$ are volume fractions for the gas and liquid phases, respectively; ρ_1, ρ_2, and ρ are densities for the gas-component, liquid-component, and mixture, respectively; u, v, and w are three components of the velocity vector $\vec{V}$ along x, y, and z axes; g is the gravitational acceleration; p is the pressure; ρE is the total energy per volume; $h=(\rho E+p)/\rho$ is the enthalpy; and K is a function given by

$$K=\alpha_1\alpha_2\left(\frac{1}{\rho_1 c_1^2}-\frac{1}{\rho_2 c_2^2}\right)\rho c^2. \tag{4}$$

For each fluid component, stiffened gas equation of state (SG-EOS) is utilised to correlate the total energy with the pressure, density, and velocity. The general form of SG-EOS is given as

$$\rho E=\frac{p+\gamma p_c}{\gamma-1}+\frac{1}{2}\rho\vec{V}^2 \tag{5}$$

in which γ is a polytropic constant and p_c is a pressure constant. The fluid mixture has two components in mechanical equilibrium (identical pressure and velocity); therefore, the total energy for the mixture is defined as

$$\begin{aligned}\rho E&=\alpha_1\rho_1E_1+\alpha_2\rho_2E_2\\ &=\alpha_1\left(\frac{p+\gamma_1 p_{c,1}}{\gamma_1-1}+\frac{1}{2}\rho_1\vec{V}^2\right)+\alpha_2\left(\frac{p+\gamma_2 p_{c,2}}{\gamma_2-1}+\frac{1}{2}\rho_2\vec{V}^2\right)\\ &=p\left(\frac{\alpha_1}{\gamma_1-1}+\frac{\alpha_2}{\gamma_2-1}\right)+\left(\frac{\alpha_1\gamma_1 p_{c,1}}{\gamma_1-1}+\frac{\alpha_2\gamma_2 p_{c,2}}{\gamma_2-1}\right)+\frac{1}{2}\rho\vec{V}^2\end{aligned} \tag{6}$$

in which the density of mixture is computed as $\rho=\alpha_1\rho_1+\alpha_2\rho_2$.

If the gravitational terms are excluded and only the x-direction is considered, 3D system (3) will reduce to the 1D model of Kapila *et al.*[33] To the knowledge of the authors, the mathematical properties of the model of Kapila *et al.* have only been analysed in one- and two-dimensional forms while an

This article is copyrighted as indicated in the article. Reuse of AIP content is subject to the terms at: http://scitation.aip.org/termsconditions. Downloaded to IP: 149.170.118.205 On: Tue, 26 Jan 2016 09:29:20

analysis of the mathematical properties of the model in 3D form together with its extension to real 3D hydrodynamic impact problems have not been reported in the literature. In the present work, a detailed analysis of the eigenstructure of system (3) in primitive form is carried out and presented in Appendix A.

Supposing the mesh does not vary with time, a finite volume discretisation of Equation (3) for a mesh cell m is given by

$$\Omega_m \frac{\mathbf{U}_m^{n+1} - \mathbf{U}_m^n}{\Delta t} + \sum_{f=1}^{N_m} \mathbf{F}_f S_f = \Omega_m \mathbf{G}_m, \tag{7}$$

where the subscript m stands for the mesh cell itself, Ω_m is the volume of the mesh cell, the subscript f represents a mesh cell face, and N_m is the total number of faces for the mesh cell. A third order monotonic upstream-centered scheme for conservation laws (MUSCL) with a slope limiter is utilised to interpolate the left- and right-side solution variables for the mesh face f. The surface flux term $\mathbf{F}_f$ is treated as a discontinuity and computed by means of a Harten-Lax-van Leer-Contact (HLLC) approximate Riemann solver. A third order total variation diminishing (TVD) Runge-Kutta scheme is applied to update the numerical solution from time level n to $n + 1$. Readers may refer to the Ref. 32 for more details.

The hydro-code's capability properly to handle the compressibility of air and water-air mixture has been verified through a series of benchmark test cases including 1D gravity-induced liquid piston, water-air shock tube, free drop of a water column in a closed 2D tank, slamming of a 2D flat plate into pure water, and plunging wave impact at a vertical wall reported in our recent work.[32] Here, we extend the numerical model to solve practical 3D hydrodynamic impact problems.

IV. RESULTS AND DISCUSSION

In the laboratory, the drop height of the plate is calibrated to obtain impact velocities 5.5 m/s and 7 m/s while the present numerical model is constructed in the Eulerian frame of reference consistent with a finite volume method. To solve the water entry problem, we fix the flat plate in the numerical mesh and cause the water to move upward with the prescribed impact velocity. This strategy is appropriate for a short-duration impact process.[34] Since violent hydrodynamic impacts are usually inertia dominant, viscous effects are currently ignored in the numerical computation. Therefore, a compatible no-penetration velocity boundary condition should be applied at the flat plate.

Before the trapped air layer breaks into small bubbles, turbulence does not play a significant role in the impact process, thus the flow could reasonably be assumed to be symmetric about the two central sections of the plate. Consequently, we compute only a quarter of the whole flow field chosen as a cubic region $[0, 0.4] \times [0, 0.4] \times [0, 0.4]$ (x–y–z, unit m) to cover a quarter of the plate located in the region $[0, 0.125] \times [0.2, 0.212] \times [0, 0.125]$ (x–y–z, unit m). The thickness of the plate is 0.012 m. The initial calm water surface is set at $y = 0.1$ m and so the distance to the plate is 0.1 m in the hydro-code. Symmetry conditions are applied at the boundaries corresponding to the central sections of the plate. The numerical domain is discretised by $80 \times 1200 \times 80$ mesh cells. The purpose of using large number of cells in y-direction is to capture as accurately as possible the peak loadings. The numerical results and experimental measurements for pure and aerated water entries are presented in the following, respectively.

A. Pure water entry

Figure 7 presents the time series of gauge pressures and total slamming force on the plate for an impact velocity $v = 5.5$ m/s. The phases of these data have been properly shifted to correlate the first pressure peak at P1 to time $t = 0$. It is clearly shown that the evolution of the impact pressure loading at the plate centre consists of distinct stages including shock loading, fluid expansion (low pressure) loading, and secondary re-loading.

When the plate approaches the water surface, the pressure rises very sharply to the first and highest peak value in less than 1 ms and then drops very quickly to zero. The first and highest pressure

This article is copyrighted as indicated in the article. Reuse of AIP content is subject to the terms at: http://scitation.aip.org/termsconditions. Downloaded to IP: 149.170.118.205 On: Tue, 26 Jan 2016 09:29:20

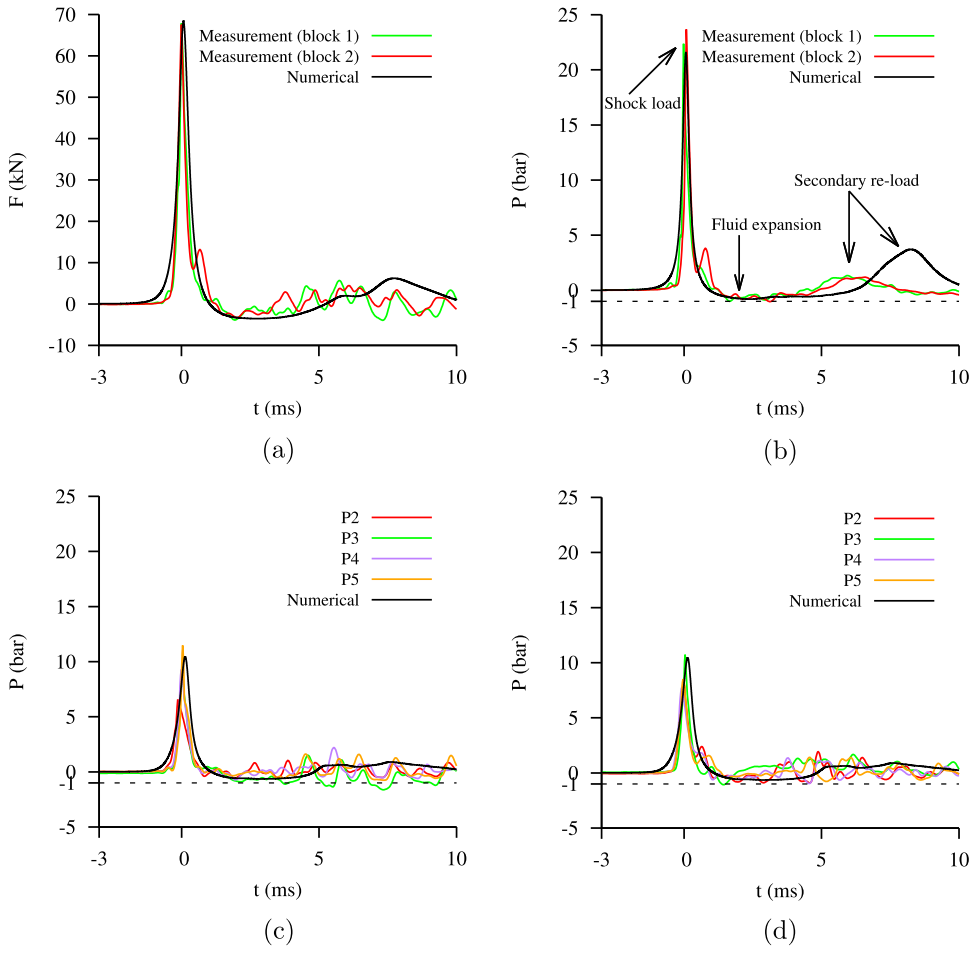

FIG. 7. Pure water slamming loads on the plate for $v = 5.5$ m/s. All the pressures presented here are gauge values. The horizontal dashed line represents a perfect vacuum pressure. Phases of all the results are adjusted to correlate the first pressure peak to time $t = 0$. The masses of blocks 1 and 2 are 32 kg and 52 kg, respectively. (a) Total force. (b) Pressure at P1. (c) Block 1, pressures at P2, 3, 4, and 5. (d) Block 2, pressures at P2, 3, 4, and 5.

spike could be considered as a shock loading.[35] The duration of the shock loading is less than 2 ms. Table I lists the peak loadings on the plate. At P1, the maximum value of the shock load is 21.57 bars for the numerical simulation and is within 22.16 bars and 23.66 bars for the laboratory measurements. At the other four symmetric gauge points P2, 3, 4, and 5, the computed peak values are 10.44 bars; the laboratory measurement shows that the data vary from 6.53 bars to 11.42 bars for block 1 and from 7.77 bars to 10.71 bars for block 2. The discrepancy between these pressure gauge measurements taken at symmetric positions on the plate may be due to plate flexure or minor variations in plate

TABLE I. Peak gauge pressures and forces on the plate for pure water entry.

v (m/s)	Instrument	P1 (bar)	P2 (bar)	P3 (bar)	P4 (bar)	P5 (bar)	F (kN)
	Block 1	22.16	6.53	8.46	9.43	11.42	68.35
5.5	Block 2	23.66	8.31	10.71	7.77	8.63	69.57
	Numerical	21.57	10.44	10.44	10.44	10.44	68.41
	Block 1	37.62	14.92	15.97	12.64	10.73	105.40
7.0	Block 2	28.47	10.26	18.54	15.29	18.43	99.93
	Numerical	35.46	17.07	17.07	17.07	17.07	124.92

This article is copyrighted as indicated in the article. Reuse of AIP content is subject to the terms at: http://scitation.aip.org/termsconditions. Downloaded to IP: 149.170.118.205 On: Tue, 26 Jan 2016 09:29:20

TABLE II. Impulses of shock loading on the plate for pure water entry. Pressure and force impulses are calculated as $P^I = \int_{t_b}^{t_a} p\,dt$ and $F^I = \int_{t_b}^{t_a} f\,dt$, respectively, where t_b and t_a are the times immediately before and after the shock loading.

v (m/s)	Instrument	P_1^I (Pa s)	P_2^I (Pa s)	P_3^I (Pa s)	P_4^I (Pa s)	P_5^I (Pa s)	F^I (N s)
	Block 1	652.46	335.21	327.90	355.95	359.73	25.27
5.5	Block 2	719.71	381.59	359.25	388.14	402.53	28.55
	Numerical	849.10	614.33	614.33	614.33	614.33	35.02
	Block 1	783.27	425.32	383.61	435.97	423.05	30.49
7.0	Block 2	851.03	515.16	487.58	514.57	491.46	35.66
	Numerical	1092.28	770.26	770.26	770.26	770.26	50.31

impact angle. Any of these factors may cause some transducers to contact the water slightly earlier than others. Regarding the total impact loading, the slamming force is positive (upward direction) with a peak value around 68.35 kN to 69.57 kN during this stage (see Table I). Just after the first peak, the measurement data for P1 also show a pressure spike up to 4.6 bars in the time series at around $t = 0.6$ ms. This spike is not captured in numerical simulation. The underlying reason that caused this small secondary pressure spike might be due to the reflection of shock (pressure wave) from the bottom of ocean basin. To justify this speculation, an analysis of the propagation time of pressure waves in the ocean basin is presented in Appendix B.

A strong burst of acoustic noise was observed in the experiments on impact which seems to be closely related to the shock loading. However, this is not the main interest of our current work and was not recorded in detail. Consequently, we are not able to accurately analyse the associated sound level.

The impulses of shock loading on the plate obtained in experiments and numerical simulations are presented in Table II. These values are calculated as temporal integrals of local pressures or overall forces through the interval $[t_b, t_a]$, which covers the lifespan of the shock load. The computed peak pressures at P1 and overall forces listed in Table I are close to the measurement for entry velocity $v = 5.5$ m/s, but the rise time is longer compared to that of experiment. Therefore, the computed impulses are greater than experiment results as shown in Table II.

After the shock load, the extensively compressed air layer trapped beneath the plate expands and induces the pressure to further decrease towards a vacuum. The lowest absolute pressure obtained in the numerical computation is 20.03 kPa at P1 and 36.15 kPa at P2 (see Table III). The measured lowest absolute pressures show a variety of values including negative and positive readings. These negative values may be due to the acoustic noise generated by the shock in the ocean basin. However, the observed trend in the measured data is close to the numerical simulation results. After the lowest value, the pressure starts to increase towards zero with a second contraction of the trapped air. At P1, the duration of the fluid expansion load is 5.2 ms for the numerical simulation and 3.5 ms ~ 3.7 ms for the experiment. At the four symmetric gauge points, the duration of the fluid expansion load is 3.7 ms for the numerical simulation and around 3.5 ms for experiment. The sub-atmospheric pressure on the lower surface causes the plate to experience negative (downward in direction) impact force for

TABLE III. Minimum absolute pressures and forces on the plate for pure water entry, $t \in [0, 5\ \text{ms}]$.

v (m/s)	Instrument	P1 (kPa)	P2 (kPa)	P3 (kPa)	P4 (kPa)	P5 (kPa)	F (kN)
	Block 1	0.59	41.74	−62.19	27.86	24.05	−3.92
5.5	Block 2	−2.67	8.81	−6.37	3.86	22.69	−3.29
	Numerical	20.03	36.15	36.15	36.15	36.15	−3.54
	Block 1	−18.92	19.78	13.85	34.68	40.16	−3.89
7.0	Block 2	0.75	27.09	18.13	12.91	13.09	−3.95
	Numerical	6.65	23.95	23.95	23.95	23.95	−4.73

This article is copyrighted as indicated in the article. Reuse of AIP content is subject to the terms at: http://scitation.aip.org/termsconditions. Downloaded to IP: 149.170.118.205 On: Tue, 26 Jan 2016 09:29:20

around 4 ms as shown in Figure 7. The computed minimum impact force on the plate is −3.54 kN, the measured data are −3.92 kN for block 1 and −3.29 kN for block 2.

When the pressure recovers from sub-atmospheric to atmospheric values, the air layer does not stop contracting but is further compressed and leads to secondary re-loading of the plate. This re-loading is less severe compared to the shock loading. At P1, the numerical simulation produces stronger re-loading (3.71 bars) compared to the laboratory measurement (1.5 bars ∼ 2 bars). This may be due to the inviscid assumption adopted in the numerical simulation, which currently ignores the fact that part of the fluid kinematic energy would be dissipated by viscosity. The amplitude of the entire re-loading (force) obtained from numerical simulation is slightly higher than that of experiments.

Snapshots of the loadings on the plate obtained by numerical simulation and/or experiment are given in Figure 8. The left side represents the solution at $t = -0.035$ ms, just before the occurrence of shock load peak. The right side indicates the result at $t = 2.365$ ms, which is at a time very close to the trough of the fluid expansion load. The time $t = 0$ corresponds to the first pressure peak at P1. The top row illustrates contours of the computed pressure distribution on the lower surface of the plate. The middle row depicts the pressure distribution along the horizontal central section of the plate (lower surface). The bottom row shows the computed velocity field at centres of the mesh cells that are just beneath the lower surface of the flat plate. At $t = -0.035$ ms, the pressure is nearly axisymmetric on the plate apart from the four corners. The computed highest absolute pressure (21.30 bars) is found to be at the plate centre and decreases outwards. The measured pressure here is 21.54 bars for block 1 and 21.95 bars for block 2. The computed lowest pressures (5.78 bars) are at the four corners of the plate. The velocity vectors are directed outward from the plate centre. This means the fluid beneath the plate is being expelled away from the plate. At $t = 2.365$ ms, the plate is experiencing non-axisymmetric sub-atmospheric pressure loading. The computed lowest pressure (0.20 bars) is at the plate centre and it increases outwards. Meanwhile, the measured pressure at the plate centre is 0.33 bars for block 1 and 0.21 bars for block 2. The computed highest pressures (1.04 bars) are at the four corners of the plate. The velocity vectors are directed inwards towards the plate centre. This indicates that ventilation may happen as the fluid is being drawn in under the plate.

Similar phenomena can be observed for the case with impact velocity $v = 7$ m/s as shown in Figures 9 and 10. However, we would like to point out that the measurement becomes more difficult with this high impact velocity. At P1, the measured peak pressure varies from 28.5 bars to 37.6 bars. The numerical simulation gives a pressure of 35.46 bars. All the results are below the acoustic pressure 105 bars predicted by von Karman's formula. At the four symmetric gauge points, the measured pressure varies from 10.3 bars to 18.5 bars. While the numerical simulation provides a solution of 17.07 bars. In general, however, the computed solution is close to experimental data considering the evolution of impact loadings. Looking at Table I, it is observed that the impact loadings increase with the entry velocity. When looking at Table III, it is interesting to find that the computed trough (minimum) impact loadings decrease with higher impact velocity. This trend is not clearly shown in the scattered measurement data.

Some researchers have claimed that cavitation occurs in hydrodynamic slamming events as the pressure descends dramatically after the shock load.[4] In the present experimental study, some transducers provide negative minimum absolute pressures; the measured positive minimum absolute pressures are within the range of 0.59 kPa to 41.74 kPa for impact velocity 5.5 m/s and 0.75 kPa to 40.16 kPa for impact velocity 7 m/s. The present minimum pressures obtained in the numerical simulations at P1 are 20.03 kPa and 6.65 kPa for impact velocities 5.5 m/s and 7 m/s, respectively. Compared to the water saturation pressure of 1.70 kPa at 15 °C, most of the valid/positive experimental data and all the numerical results are still above the cavitation condition except the lowest pressures 0.59 kPa measured at P1 of block 1 for $v = 5.5$ m/s and 0.75 kPa measured at P1 of block 2 for $v = 7$ m/s. Consequently, we are currently not able to conclude that cavitation certainly occurs in the water entry of the square plate for $v = 5.5$ m/s and 7 m/s. However, it is obvious that the computed and measured low pressures are very close to the cavitation condition, and so the surrounding water is very likely to be in tension.

The phenomenon of the three-stage hydrodynamic impact is very similar to an underwater explosion problem, which usually consists of primary shock loading, low-pressure cavitation loading, and the subsequent violent re-loading due to the collapse of cavitation.

This article is copyrighted as indicated in the article. Reuse of AIP content is subject to the terms at: http://scitation.aip.org/termsconditions. Downloaded to IP: 149.170.118.205 On: Tue, 26 Jan 2016 09:29:20

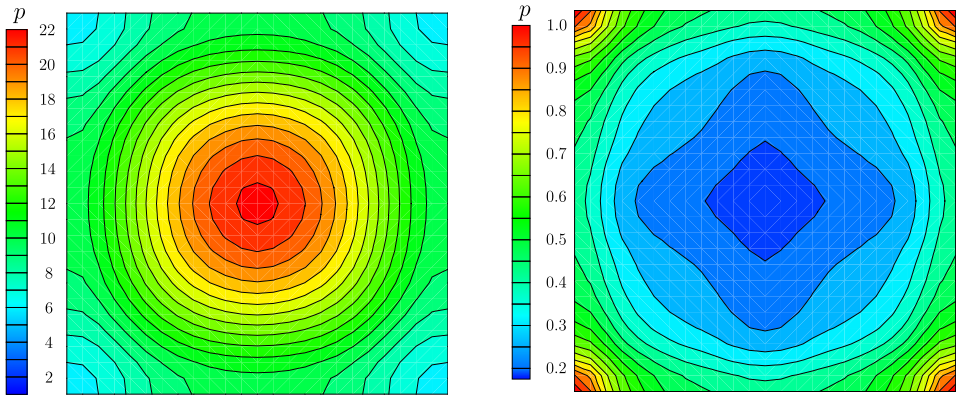

(a)

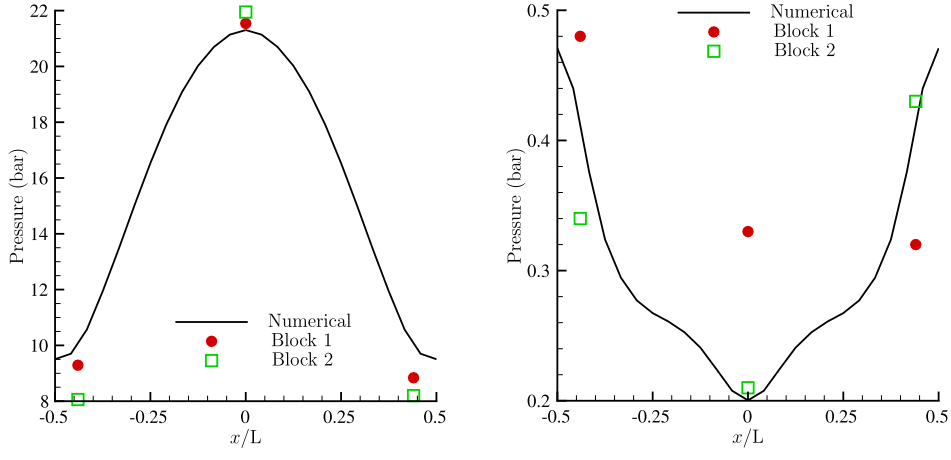

(b)

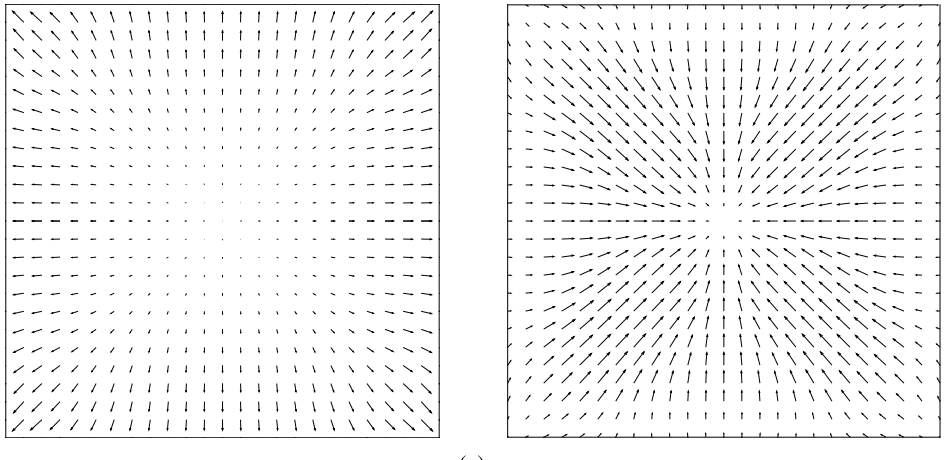

(c)

FIG. 8. Impact loadings on the flat plate at $T = -0.035$ ms (left) and $T = 2.365$ ms (right) for $v = 5.5$ m/s, pure water entry. (a) Contours of the computed absolute pressure. (Units in bar.) (b) Computed and measured pressures along the horizontal central section. (c) Computed velocity field.

A mesh convergence study of the 3D pure water entry problem reveals that the principal three stages of the impact loading could be repeatedly captured on coarser meshes though there is some discrepancy between the predicated peak values. The limitations of the present mesh for 3D problems are discussed in detail in Appendix C.

This article is copyrighted as indicated in the article. Reuse of AIP content is subject to the terms at: http://scitation.aip.org/termsconditions. Downloaded to IP: 149.170.118.205 On: Tue, 26 Jan 2016 09:29:20

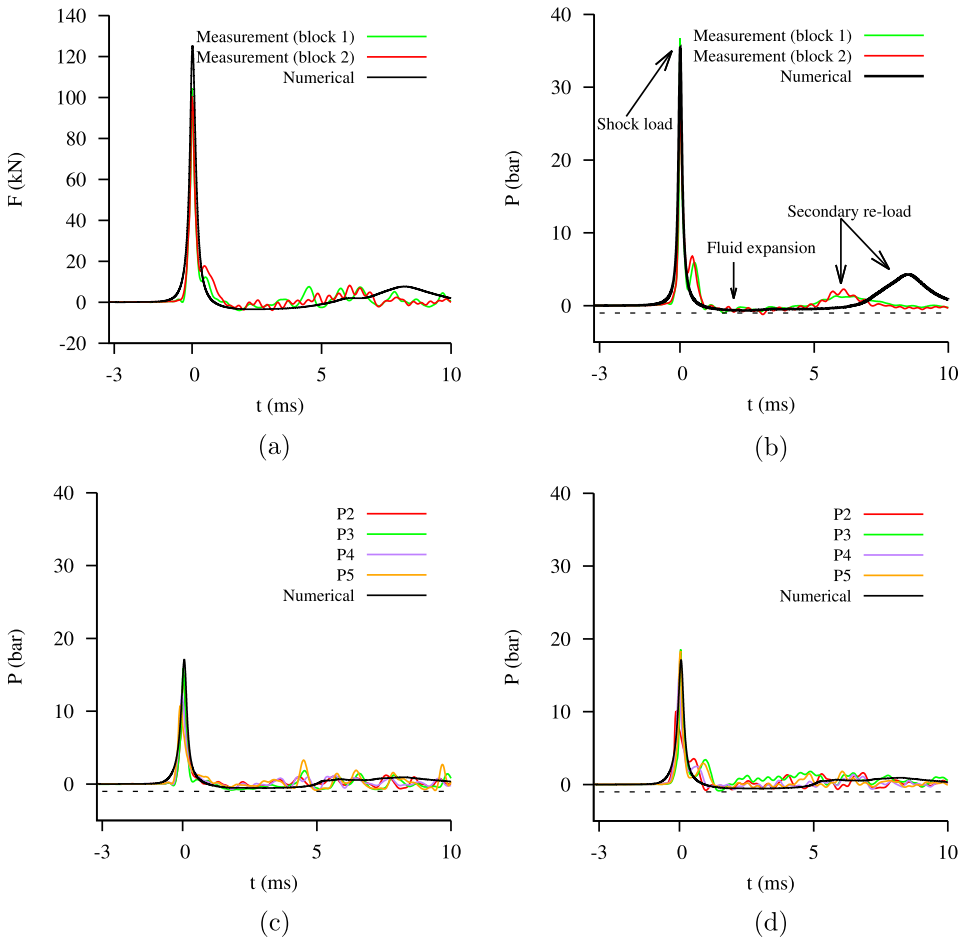

FIG. 9. Impact loadings on the plate for $v = 7$ m/s. The horizontal dashed line represents a perfect vacuum pressure. Phases of all the results are adjusted to correlate the first pressure peak to time zero. The masses of blocks 1 and 2 are 32 kg and 52 kg, respectively. (a) Force. (b) Pressure (P1). (c) Block 1, pressures at P2, 3, 4, and 5. (d) Block 2, pressures at P2, 3, 4, and 5.

B. Aerated water entry

As the shock load is the most severe and dangerous to the flat plate structure, here we focus on investigating effect of aeration on the first peak loading. Before presenting the results for aerated water entry, it is necessary to clarify the differences in introducing air bubbles into the water between the experiment and the numerical computations.

In the laboratory, the bubble generation system was placed at the bottom of ocean basin, which is filled with fresh water for a depth of 1 m. The air bubbles rise from the bottom of the ocean basin to the water surface and break up. The size of the bubbles significantly increases as they ascend. Therefore, the aeration level near the water surface is notably higher than that at the bottom of basin. In the present work, the bubble aeration was measured at one water depth only (0.25 m away from the water surface) and assumed uniform throughout depth.

The numerical model does not treat the air bubbles explicitly in a one-by-one manner but instead assumes the water to be uniformly mixed with air bubbles at a specified concentration level (and thus implied speed of sound). Thus, the aeration level is represented by the air volume fraction α_1 in Equation (3). As the change of aeration level with water depth $\alpha_1(y)$ is currently not available, we apply the average representative value measured in laboratory to set up the initial conditions for the numerical computations and assume that $\alpha_1(y)$ does not vary with the water depth. Obviously, this is a simplified and conservative treatment as the real aeration level near the water surface is notably under-estimated in the numerical model's setup.

This article is copyrighted as indicated in the article. Reuse of AIP content is subject to the terms at: http://scitation.aip.org/termsconditions. Downloaded to IP: 149.170.118.205 On: Tue, 26 Jan 2016 09:29:20

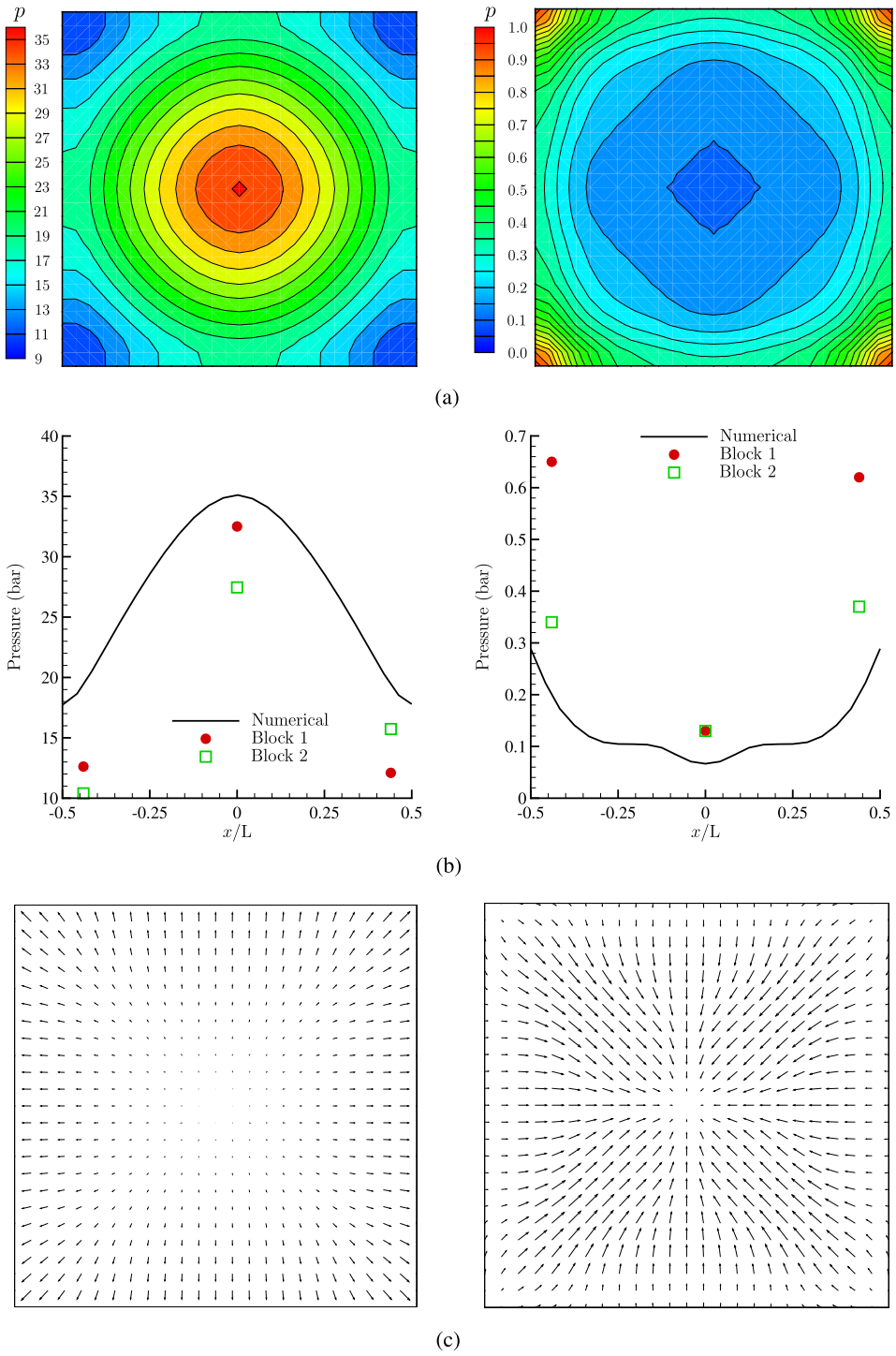

FIG. 10. Impact loadings on the flat plate for $v = 7$ m/s, pure water entry. Left: $T = -0.013$ ms, just before the first pressure peak; right: $T = 2.487$ ms, near the occurrence of pressure trough. (a) Contours of the computed absolute pressures. (Units in bar.) (b) Computed and measured pressures along the horizontal central section. (c) Computed velocity field.

Figures 11 and 12 show the time series of the gauge pressures on the plate under different aeration levels for impact velocities 5.5 m/s and 7 m/s, respectively. The left column represents the pressures measured for block 1 (32 kg), the middle column indicates the data for block 2 (52 kg), and the right column illustrates the numerical results. From the top to bottom rows are the pressures

This article is copyrighted as indicated in the article. Reuse of AIP content is subject to the terms at: http://scitation.aip.org/termsconditions. Downloaded to IP: 149.170.118.205 On: Tue, 26 Jan 2016 09:29:20

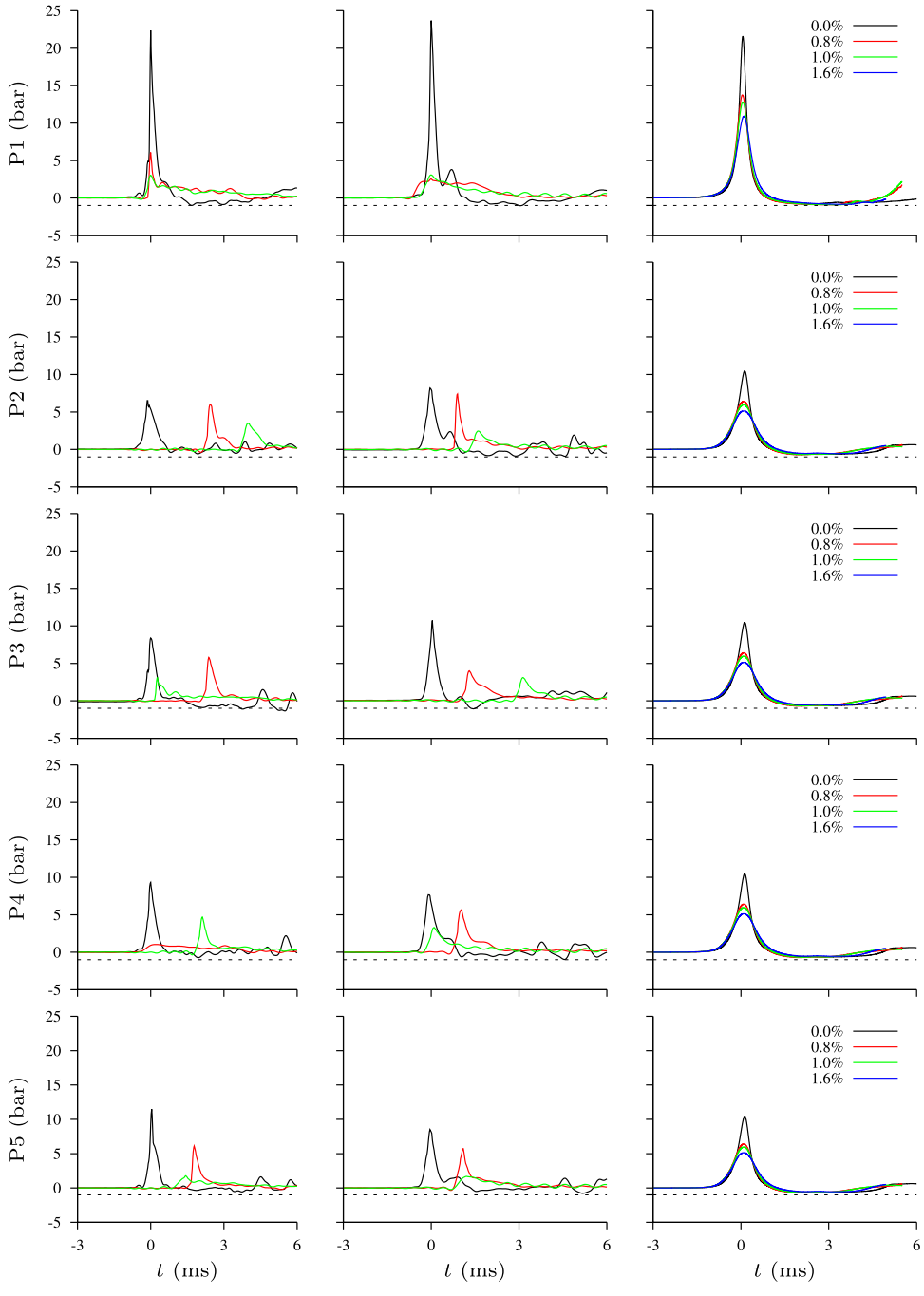

FIG. 11. Impact pressures on the plate in water with different aeration levels ($\alpha_1 = 0\%$–1.6%) for $v = 5.5$ m/s. Left: block 1 (32 kg); middle: block 2 (52 kg); right: numerical computation. From the top to bottom rows are the pressures at gauge points P1, 2, 3, 4, and 5. The computed results at P2, 3, 4, and 5 are identical.

gauged/computed at locations P1, 2, 3, 4, and 5. Please note that all the time series have been shifted to correlate the first peak of P1 to time $t = 0$.

Close inspection of these two figures shows that the peak impact pressures on the plate are significantly reduced by aeration. In the numerical computation, at all gauge points, the pressures are continuously reduced by increased aeration levels. The highest aeration level $\alpha_1 = 1.6\%$ reduces all the pressures by 49.4%–50.7% for $v = 5.5$ m/s and 43.3%–48.2% for $v = 7$ m/s. Looking at the

This article is copyrighted as indicated in the article. Reuse of AIP content is subject to the terms at: http://scitation.aip.org/termsconditions. Downloaded to IP: 149.170.118.205 On: Tue, 26 Jan 2016 09:29:20

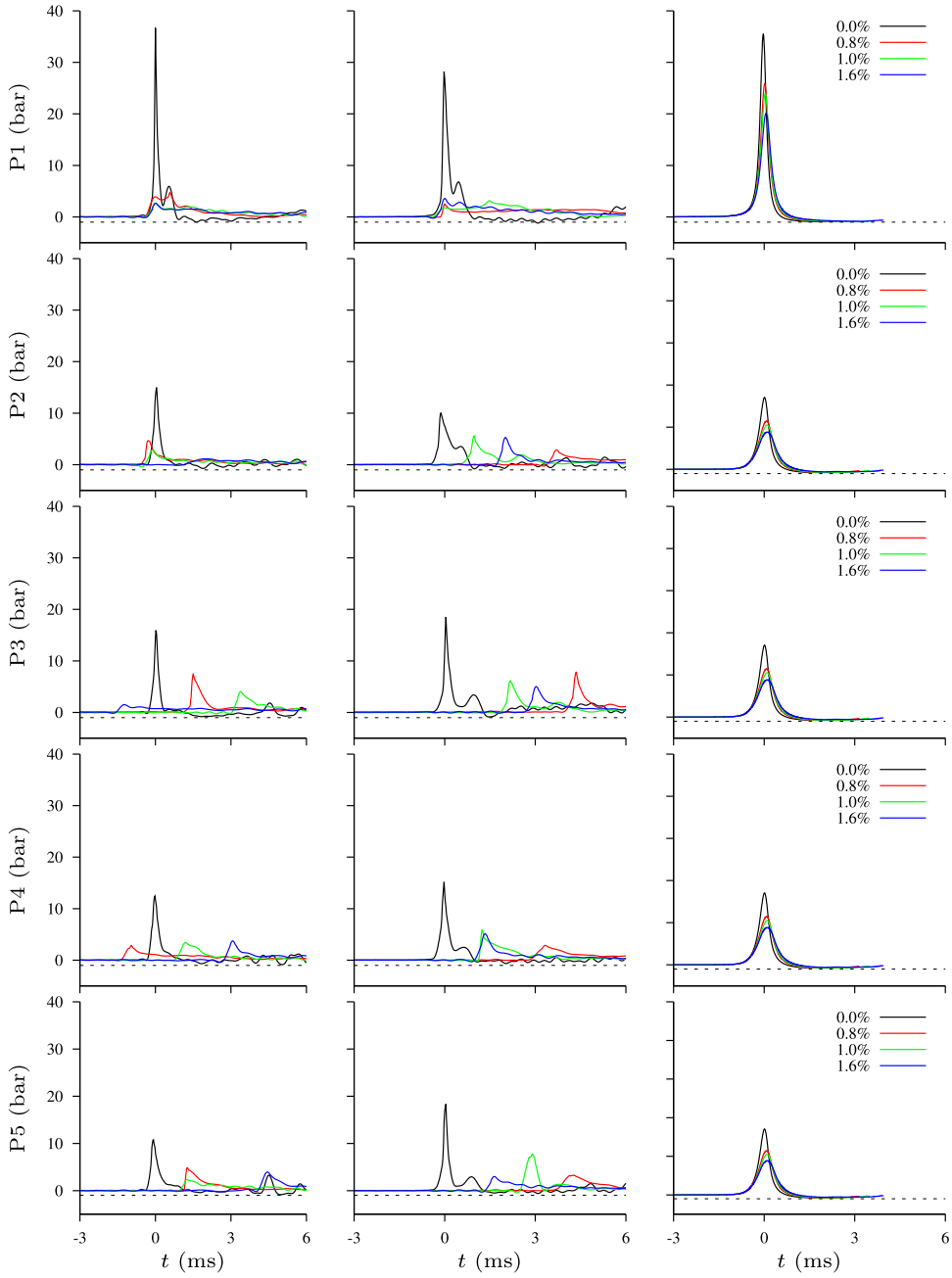

FIG. 12. Impact pressures on the plate in water with different aeration levels ($\alpha_1 = 0\%$–1.6%) for $v = 7$ m/s. Left: block 1 (32 kg); middle: block 2 (52 kg); right: numerical computation. From the top to bottom rows are the pressures at gauge points P1, 2, 3, 4, and 5. The computed results at P2, 3, 4, and 5 are identical.

measurement data, the reduction in pressure is greater when the same level of aeration is used. Here, we would like to emphasise again that the aeration level near the water surface is noticeably higher than that of the basin bottom. In the experiment, the aeration levels were measured at only one depth with a distance of 0.25 m away from the water surface. Since the real aeration near the water surface is higher than the measurement point, we only implement the significant average measurement value, which is rather conservative/under-estimated, in the numerical simulation.

Looking at the measured pressures at P2, 3, 4, and 5 shown in Figures 11 and 12, it is easy to spot that the occurrences of the pressure peaks are notably non-synchronous with P1 by phase shifts up

This article is copyrighted as indicated in the article. Reuse of AIP content is subject to the terms at: http://scitation.aip.org/termsconditions. Downloaded to IP: 149.170.118.205 On: Tue, 26 Jan 2016 09:29:20

TABLE IV. Maximum gauge pressures and forces on the plate for aerated water entry.

v (m/s)	Instrument	α_1 (%)	P1 (bar)	P2 (bar)	P3 (bar)	P4 (bar)	P5 (bar)	F (kN)
5.5	Block 1	0.0	22.16	6.53	8.46	9.43	11.42	68.35
		0.8	6.35	6.40	6.14	2.47	6.23	18.55
		1.0	3.77	3.86	3.87	4.82	1.93	12.11
		1.6	...	...	...	...	...	...
	Block 2	0.0	23.66	8.31	10.71	7.77	8.63	69.57
		0.8	2.89	7.50	3.94	6.08	6.27	21.69
		1.0	3.67	3.97	4.03	4.12	2.92	15.87
		1.6	...	...	...	...	...	...
	Numerical	0.0	21.57	10.44	10.44	10.44	10.44	68.41
		0.8	13.75	6.41	6.41	6.41	6.41	46.65
		1.0	12.81	5.97	5.97	5.97	5.97	43.72
		1.6	10.92	5.14	5.14	5.14	5.14	37.76
7.0	Block 1	0.0	37.62	14.92	15.97	12.64	10.73	105.40
		0.8	5.15	4.76	7.44	3.27	5.08	20.35
		1.0	3.51	3.14	6.53	4.10	3.57	24.85
		1.6	3.43	3.27	3.09	5.57	5.29	22.02
	Block 2	0.0	28.47	10.26	18.54	15.29	18.43	99.93
		0.8	2.83	3.07	8.36	2.93	3.85	22.65
		1.0	3.39	5.70	6.19	6.14	8.03	17.80
		1.6	4.89	5.61	5.87	6.58	3.53	19.37
	Numerical	0.0	35.46	17.07	17.07	17.07	17.07	124.92
		0.8	25.80	11.45	11.45	11.45	11.45	83.32
		1.0	23.98	10.51	10.51	10.51	10.51	77.52
		1.6	20.09	8.84	8.84	8.84	8.84	66.28

to 4.2 ms. In the experiment, the water surface is not flat for the aerated cases due to the disturbance caused by rising bubbles, and the surface disturbance is greater for higher aeration levels. Therefore, the pressure transducers installed on the plate are not in contact with the water surface at the same time. While in the numerical simulation, the surface is assumed to be flat. This leads to the significant difference in phase and amplitude of the pressure peaks.

The details of peak pressures as well as impact forces measured/computed under different aeration levels and impact velocities are listed in Table IV. The computed minimum absolute pressures and forces under different aeration levels and impact velocities are listed in Table V.

Figures 13 and 14 show the computed pressures on the plate near the occurrence of peak loading and trough loading in 0.8% aerated water for $v = 5.5$ m/s and 7 m/s, respectively. Similar to the pure

TABLE V. Computed minimum absolute pressures and forces on the plate for aerated water entry.

v (m/s)	α_1 (%)	P1 (kPa)	P2 (kPa)	P3 (kPa)	P4 (kPa)	P5 (kPa)	F (kN)
5.5	0.0	20.03	36.15	36.15	36.15	36.15	−3.54
	0.8	8.67	28.79	28.79	28.79	28.79	−4.34
	1.0	9.56	32.47	32.47	32.47	32.47	−4.21
	1.6	14.61	44.72	44.72	44.72	44.72	−3.65
7.0	0.0	6.65	23.95	23.95	23.95	23.95	−4.73
	0.8	6.85	24.23	24.23	24.23	24.23	−5.35
	1.0	7.87	28.99	28.99	28.99	28.99	−5.15
	1.6	14.51	40.88	40.88	40.88	40.88	−4.36

This article is copyrighted as indicated in the article. Reuse of AIP content is subject to the terms at: http://scitation.aip.org/termsconditions. Downloaded to IP: 149.170.118.205 On: Tue, 26 Jan 2016 09:29:20

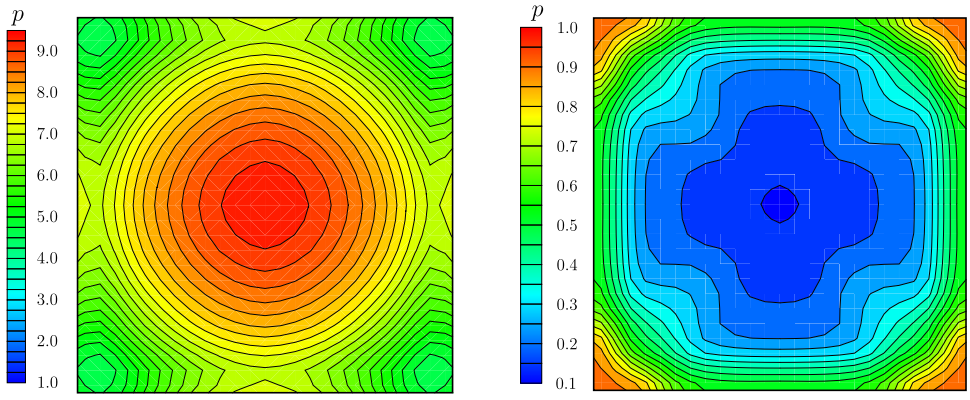

(a) (b)

FIG. 13. Computed contours of absolute pressures (units in bar) on the plate for $v = 5.5$ m/s and aeration level 0.8%. Left: $t = 0.18$ ms, just after the occurrence of peak loading at P1; right: $t = 3.18$ ms, near the occurrence of trough loading at P1. (a) $t = 0.180$ ms. (b) $t = 3.180$ ms.

water entry cases, at the time near the occurrence of peak loading, the pressure distribution on the plate is nearly axisymmetric apart from the four corners. At the time near the occurrence of trough loading, the pressure distribution is non-axisymmetric. The trapped air undergoes intensive compression and expansion. The pressure distribution for cases with higher aeration levels is similar to these two figures (except the amplitude of pressure); therefore, they are not included here.

Figures 15 and 16 show the peak pressures at P1 and total impact forces on the plate for pure and aerated water entries obtained in experiment and numerical simulations. All the numerical results indicate that both the pressure and force decline with increased aeration levels. When bubbles are generated to aerate the fresh water in laboratory, the water surface is greatly disturbed by the quickly rising and breaking bubbles. This causes some difficulty in measuring impact loadings and leads to obvious phase shifts of pressure peaks. Nevertheless, the experimental data illustrate that aeration can dramatically reduce the peak loadings.

Figures 17 and 18 show the impulses of shock loading on the plate for entry into pure and aerated water. These impulses are calculated as time integrals of pressure or force in the interval $[t_b, t_a]$, which covers the lifespan/duration of the shock load. Looking at the pressure impulse at P1, the numerical simulation shows a declining trend with increased aeration level (but the reduction is mild compared to the reduction of peak pressures); the experiment does not clearly show this declining trend. Looking

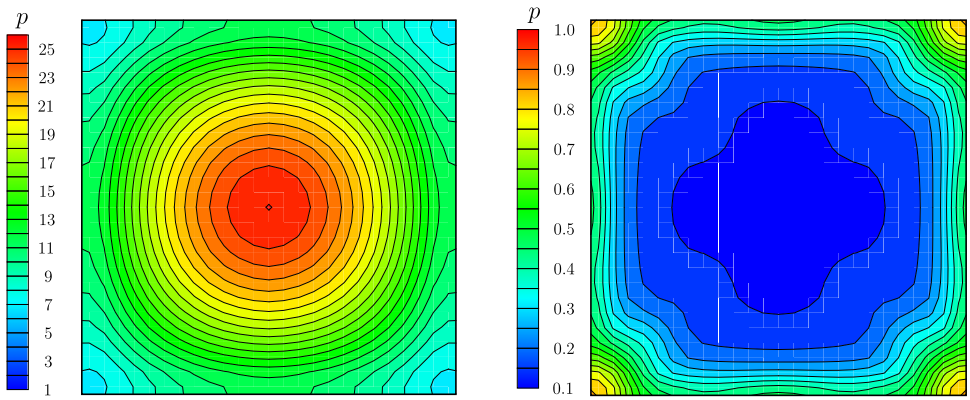

(a) (b)

FIG. 14. Computed contours of absolute pressures (units in bar) on the plate for $v = 7$ m/s and aeration level 0.8%. Left: $t = 0.023$ ms, just after the occurrence of peak loading at P1; right: $t = 5.177$ ms, near the occurrence of trough loading at P1.

This article is copyrighted as indicated in the article. Reuse of AIP content is subject to the terms at: http://scitation.aip.org/termsconditions. Downloaded to IP: 149.170.118.205 On: Tue, 26 Jan 2016 09:29:20

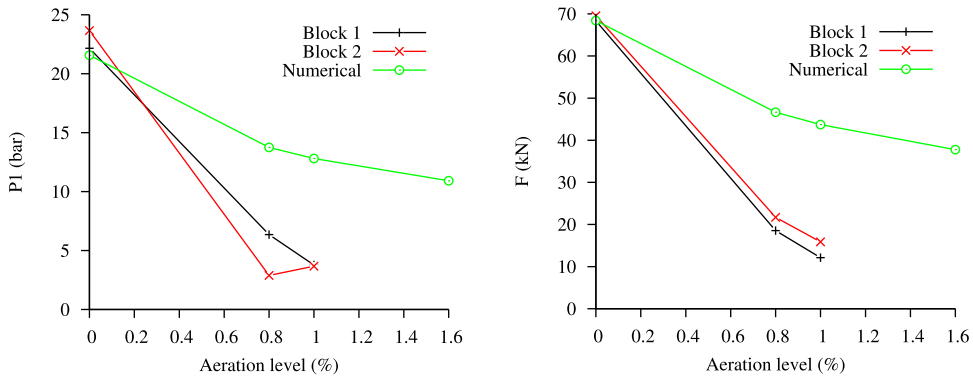

FIG. 15. Aeration effects on the peak impact loadings for $v = 5.5$ m/s. Left: peak gauge pressure at P1; right: total impact force on the plate.

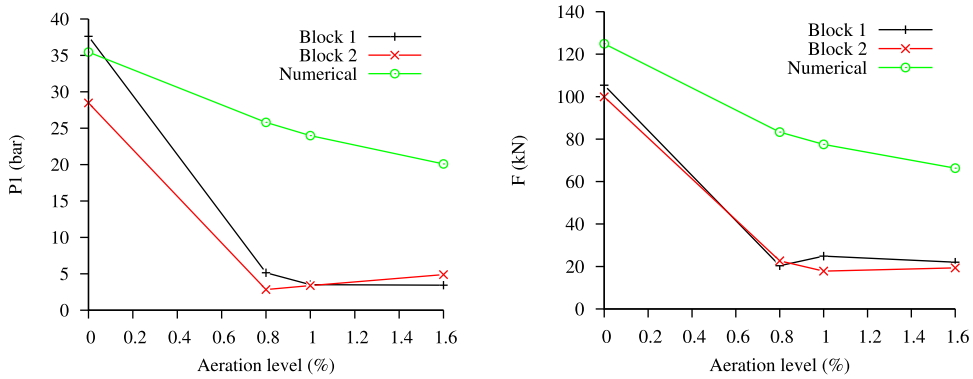

FIG. 16. Aeration effects on the peak impact loadings for $v = 7$ m/s. Left: peak gauge pressure at P1; right: total impact force on the plate.

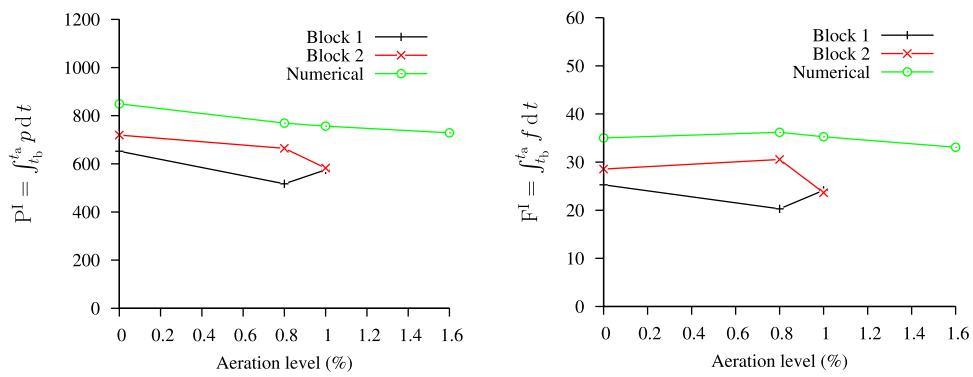

FIG. 17. Aeration effects on the impulse of shock loadings for $v = 5.5$ m/s. Left: pressure impulse at P1; (units in Pa s) right: total force impulse on the plate (units in N s).

at the force impulse on the plate, neither numerical computation nor experiment shows a clear declining or rising trend; the force impulse experiences both rise and decline. The difference in shock load impulse between pure water and aerated water with highest aeration level is presented in Table VI. For pressure impulse at P1, the maximum aeration level seems to be able to reduce it by 7.1%–19.1% (only one exception: 3.1% increase on block 2 for $v = 7$ m/s). Meanwhile the maximum aeration level causes up to 17.2% variation of force impulse.

This article is copyrighted as indicated in the article. Reuse of AIP content is subject to the terms at: http://scitation.aip.org/termsconditions. Downloaded to IP: 149.170.118.205 On: Tue, 26 Jan 2016 09:29:20

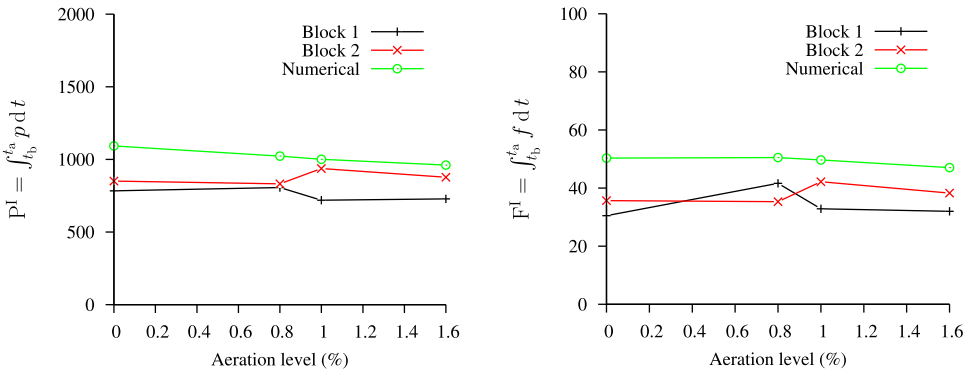

FIG. 18. Aeration effects on the impulse of shock loadings for $v = 7$ m/s. Left: pressure impulse at P1; (units in Pa s) right: total force impulse on the plate (units in N s).

TABLE VI. Variation of shock load impulse between pure water impact and aerated water (with highest aeration level) impact.

		P_1^I (Pa s)			F^I (N s)		
v (m/s)	Instrument	$\alpha_1 = 0$	max(α_1)	ΔP_1^I (%)	$\alpha_1 = 0$	max(α_1)	ΔF^I (%)
	Block 1	652.46	574.85	−11.9	25.27	24.13	−4.5
5.5	Block 2	719.71	582.58	−19.1	28.55	23.65	−17.2
	Numerical	849.10	728.90	−14.2	35.02	33.08	−5.5
	Block 1	783.27	727.80	−7.1	30.49	31.98	+4.9
7.0	Block 2	851.03	877.66	+3.1	35.66	38.28	+7.3
	Numerical	1092.28	961.07	−12.0	50.31	47.04	−6.5

V. CONCLUSIONS

The experimental and numerical study reveals that the impact loadings on the square rigid plate during water entry consists of distinct features including (1) shock loading with the highest observed peak pressure, (2) fluid expansion loading with very low sub-atmospheric pressure, and (3) less severe secondary reloading with super-atmospheric pressure. For high speed pure water impacts ($v \geq 5$ m/s), the duration of the shock loading is less than 2 ms, and it is around 4 ms for the low pressure loading. The minimum values for all the computed pressures and most of the measured positive pressures are very close to (though still above) the saturated vapour pressure. Therefore, the surrounding water is very likely to be in tension near the cavitation condition.

The experiments and numerical computations also show that the peak loading on the flat plate can be effectively reduced by half or even more with 1.6% aeration in water. Compared to pure water condition, aeration increases the rise and/or fall time of the shock load. This means that the shock loading in aerated water has a longer lifespan and the resulting impulse is not necessarily much smaller than pure water impact. The variation of impulses is less sensitive to the change of aeration than peak loadings.

In future, we plan to carry out experiments and numerical simulations for more complex objects including an aircraft fuselage, ship configurations, and a human body model with consideration of material properties and structural elasticity. In addition to the major concern of the loadings, water entry of the flat plate is also noted to be associated with a strong acoustic noise. This deserves further investigation through experiment by detailed recording and numerical simulation by enhanced acoustics computation to carefully analyse the related acoustic characteristics.

This article is copyrighted as indicated in the article. Reuse of AIP content is subject to the terms at: http://scitation.aip.org/termsconditions. Downloaded to IP: 149.170.118.205 On: Tue, 26 Jan 2016 09:29:20

ACKNOWLEDGMENTS

This research was supported by the Engineering and Physical Sciences Research Council (EPSRC), U.K. Project: FROTH (Fundamentals and Reliability of Offshore Structure Hydrodynamics), under Grant Nos. EP/J012866/1 and EP/J012793/1. The MMU team was also partially supported by EPSRC through Grant Nos. EP/J010197/1 and EP/K037889/1.

APPENDIX A: EIGENSTRUCTURE OF THE NUMERICAL MODEL

In this section, we derive expressions for the eigenvalues and eigenvectors of three-dimensional system (3) in primitive form. Introducing a vector of primitive variables $\mathbf{W} = (\alpha_1, \rho_1, \rho_2, u, v, w, p)^{\mathrm{T}}$ and ignoring the source terms, system (3) can be written as

$$\frac{\partial \mathbf{W}}{\partial t} + \mathbf{A}\frac{\partial \mathbf{W}}{\partial x} + \mathbf{B}\frac{\partial \mathbf{W}}{\partial y} + \mathbf{C}\frac{\partial \mathbf{W}}{\partial z} = 0, \tag{A1}$$

where the matrix $\mathbf{A}$ is defined as

$$\mathbf{A} = \begin{bmatrix} u & 0 & 0 & 0 & 0 & 0 & 0 \\ 0 & u & 0 & \rho_1 & 0 & 0 & 0 \\ 0 & 0 & u & \rho_2 & 0 & 0 & 0 \\ 0 & 0 & 0 & u & 0 & 0 & 1/\rho \\ 0 & 0 & 0 & 0 & u & 0 & 0 \\ 0 & 0 & 0 & 0 & 0 & u & 0 \\ 0 & 0 & 0 & \rho c^2 & 0 & 0 & u \end{bmatrix}, \tag{A2}$$

the matrix $\mathbf{B}$ is given by

$$\mathbf{B} = \begin{bmatrix} v & 0 & 0 & 0 & 0 & 0 & 0 \\ 0 & v & 0 & 0 & \rho_1 & 0 & 0 \\ 0 & 0 & v & 0 & \rho_2 & 0 & 0 \\ 0 & 0 & 0 & v & 0 & 0 & 0 \\ 0 & 0 & 0 & 0 & v & 0 & 1/\rho \\ 0 & 0 & 0 & 0 & 0 & v & 0 \\ 0 & 0 & 0 & 0 & \rho c^2 & 0 & v \end{bmatrix}, \tag{A3}$$

and the matrix $\mathbf{C}$ is

$$\mathbf{C} = \begin{bmatrix} w & 0 & 0 & 0 & 0 & 0 & 0 \\ 0 & w & 0 & 0 & 0 & \rho_1 & 0 \\ 0 & 0 & w & 0 & 0 & \rho_2 & 0 \\ 0 & 0 & 0 & w & 0 & 0 & 0 \\ 0 & 0 & 0 & 0 & w & 0 & 0 \\ 0 & 0 & 0 & 0 & 0 & w & 1/\rho \\ 0 & 0 & 0 & 0 & 0 & \rho c^2 & w \end{bmatrix}. \tag{A4}$$

First, let us focus on the matrix $\mathbf{A}$. To obtain its eigenvalues, we first calculate the characteristic polynomial and obtain the following:

$$|\lambda \mathbf{I} - \mathbf{A}| = (\lambda - u + c)(\lambda - u)^5(\lambda - u - c). \tag{A5}$$

Let $|\lambda \mathbf{I} - \mathbf{A}| = 0$; therefore, $\mathbf{A}$ has seven real eigenvalues given by

$$\lambda_{1,\mathbf{A}} = u - c, \quad \lambda_{2,\mathbf{A}} = \lambda_{3,\mathbf{A}} = \lambda_{4,\mathbf{A}} = \lambda_{5,\mathbf{A}} = \lambda_{6,\mathbf{A}} = u, \quad \lambda_{7,\mathbf{A}} = u + c. \tag{A6}$$

This article is copyrighted as indicated in the article. Reuse of AIP content is subject to the terms at: http://scitation.aip.org/termsconditions. Downloaded to IP: 149.170.118.205 On: Tue, 26 Jan 2016 09:29:20

A corresponding set of linearly independent right eigenvectors $\mathbf{r}_i (i = 1, \ldots, 7)$ which satisfy the relation $\mathbf{A}\,\mathbf{r}_i = \lambda_{i,\mathbf{A}}\mathbf{r}_i$ can be chosen as

$$\mathbf{r}_{1,\mathbf{A}} = \begin{bmatrix} 0 \\ -\rho_1 \\ -\rho_2 \\ c \\ 0 \\ 0 \\ -\rho c^2 \end{bmatrix}, \mathbf{r}_{2,\mathbf{A}} = \begin{bmatrix} 1 \\ 0 \\ 0 \\ 0 \\ 0 \\ 0 \\ 0 \end{bmatrix}, \mathbf{r}_{3,\mathbf{A}} = \begin{bmatrix} 0 \\ 1 \\ 0 \\ 0 \\ 0 \\ 0 \\ 0 \end{bmatrix}, \mathbf{r}_{4,\mathbf{A}} = \begin{bmatrix} 0 \\ 0 \\ 1 \\ 0 \\ 0 \\ 0 \\ 0 \end{bmatrix}, \mathbf{r}_{5,\mathbf{A}} = \begin{bmatrix} 0 \\ 0 \\ 0 \\ 0 \\ 1 \\ 0 \\ 0 \end{bmatrix}, \mathbf{r}_{6,\mathbf{A}} = \begin{bmatrix} 0 \\ 0 \\ 0 \\ 0 \\ 0 \\ 1 \\ 0 \end{bmatrix}, \mathbf{r}_{7,\mathbf{A}} = \begin{bmatrix} 0 \\ \rho_1 \\ \rho_2 \\ c \\ 0 \\ 0 \\ \rho c^2 \end{bmatrix}. \quad \text{(A7)}$$

In addition, we can obtain the left eigenvectors $\mathbf{k}_i (i = 1, \ldots, 7)$ from equations $\mathbf{k}_i\,\mathbf{A} = \lambda_i \mathbf{k}_i$,

$$\mathbf{K}_{\mathbf{A}} = [\mathbf{k}_{i,\mathbf{A}}] = \begin{bmatrix} \mathbf{k}_{1,\mathbf{A}} \\ \mathbf{k}_{2,\mathbf{A}} \\ \mathbf{k}_{3,\mathbf{A}} \\ \mathbf{k}_{4,\mathbf{A}} \\ \mathbf{k}_{5,\mathbf{A}} \\ \mathbf{k}_{6,\mathbf{A}} \\ \mathbf{k}_{7,\mathbf{A}} \end{bmatrix} = \begin{bmatrix} 0 & 0 & 0 & 1/2c & 0 & 0 & -1/2\rho c^2 \\ 1 & 0 & 0 & 0 & 0 & 0 & 0 \\ 0 & 1 & 0 & 0 & 0 & 0 & -\rho_1/\rho c^2 \\ 0 & 0 & 1 & 0 & 0 & 0 & -\rho_2/\rho c^2 \\ 0 & 0 & 0 & 0 & 1 & 0 & 0 \\ 0 & 0 & 0 & 0 & 0 & 1 & 0 \\ 0 & 0 & 0 & 1/2c & 0 & 0 & 1/2\rho c^2 \end{bmatrix}. \quad \text{(A8)}$$

Similarly, we can obtain the eigenvalues for matrix $\mathbf{B}$,

$$\lambda_{1,\mathbf{B}} = v - c, \quad \lambda_{2,\mathbf{B}} = \lambda_{3,\mathbf{B}} = \lambda_{4,\mathbf{B}} = \lambda_{5,\mathbf{B}} = \lambda_{6,\mathbf{B}} = v, \quad \lambda_{7,\mathbf{B}} = v + c, \quad \text{(A9)}$$

its right eigenvectors are

$$\mathbf{r}_{1,\mathbf{B}} = \begin{bmatrix} 0 \\ -\rho_1 \\ -\rho_2 \\ 0 \\ c \\ 0 \\ -\rho c^2 \end{bmatrix}, \mathbf{r}_{2,\mathbf{B}} = \begin{bmatrix} 1 \\ 0 \\ 0 \\ 0 \\ 0 \\ 0 \\ 0 \end{bmatrix}, \mathbf{r}_{3,\mathbf{B}} = \begin{bmatrix} 0 \\ 1 \\ 0 \\ 0 \\ 0 \\ 0 \\ 0 \end{bmatrix}, \mathbf{r}_{4,\mathbf{B}} = \begin{bmatrix} 0 \\ 0 \\ 1 \\ 0 \\ 0 \\ 0 \\ 0 \end{bmatrix}, \mathbf{r}_{5,\mathbf{B}} = \begin{bmatrix} 0 \\ 0 \\ 0 \\ 1 \\ 0 \\ 0 \\ 0 \end{bmatrix}, \mathbf{r}_{6,\mathbf{B}} = \begin{bmatrix} 0 \\ 0 \\ 0 \\ 0 \\ 0 \\ 1 \\ 0 \end{bmatrix}, \mathbf{r}_{7,\mathbf{B}} = \begin{bmatrix} 0 \\ \rho_1 \\ \rho_2 \\ 0 \\ c \\ 0 \\ \rho c^2 \end{bmatrix}, \quad \text{(A10)}$$

and its left eigenvectors are

$$\mathbf{K}_{\mathbf{B}} = [\mathbf{k}_{i,\mathbf{B}}] = \begin{bmatrix} \mathbf{k}_{1,\mathbf{B}} \\ \mathbf{k}_{2,\mathbf{B}} \\ \mathbf{k}_{3,\mathbf{B}} \\ \mathbf{k}_{4,\mathbf{B}} \\ \mathbf{k}_{5,\mathbf{B}} \\ \mathbf{k}_{6,\mathbf{B}} \\ \mathbf{k}_{7,\mathbf{B}} \end{bmatrix} = \begin{bmatrix} 0 & 0 & 0 & 0 & 1/2c & 0 & -1/2\rho c^2 \\ 1 & 0 & 0 & 0 & 0 & 0 & 0 \\ 0 & 1 & 0 & 0 & 0 & 0 & -\rho_1/\rho c^2 \\ 0 & 0 & 1 & 0 & 0 & 0 & -\rho_2/\rho c^2 \\ 0 & 0 & 0 & 1 & 0 & 0 & 0 \\ 0 & 0 & 0 & 0 & 0 & 1 & 0 \\ 0 & 0 & 0 & 0 & 1/2c & 0 & 1/2\rho c^2 \end{bmatrix}. \quad \text{(A11)}$$

For matrix $\mathbf{C}$, its eigenvalues are

$$\lambda_{1,C} = w - c, \quad \lambda_{2,C} = \lambda_{3,C} = \lambda_{4,C} = \lambda_{5,C} = \lambda_{6,C} = w, \quad \lambda_{7,C} = w + c, \quad \text{(A12)}$$

This article is copyrighted as indicated in the article. Reuse of AIP content is subject to the terms at: http://scitation.aip.org/termsconditions. Downloaded to IP: 149.170.118.205 On: Tue, 26 Jan 2016 09:29:20

the right eigenvectors are

$$\mathbf{r}_{1,\mathbf{C}} = \begin{bmatrix} 0 \\ -\rho_1 \\ -\rho_2 \\ 0 \\ 0 \\ c \\ -\rho c^2 \end{bmatrix}, \mathbf{r}_{2,\mathbf{C}} = \begin{bmatrix} 1 \\ 0 \\ 0 \\ 0 \\ 0 \\ 0 \\ 0 \end{bmatrix}, \mathbf{r}_{3,\mathbf{C}} = \begin{bmatrix} 0 \\ 1 \\ 0 \\ 0 \\ 0 \\ 0 \\ 0 \end{bmatrix}, \mathbf{r}_{4,\mathbf{C}} = \begin{bmatrix} 0 \\ 0 \\ 1 \\ 0 \\ 0 \\ 0 \\ 0 \end{bmatrix}, \mathbf{r}_{5,\mathbf{C}} = \begin{bmatrix} 0 \\ 0 \\ 0 \\ 1 \\ 0 \\ 0 \\ 0 \end{bmatrix}, \mathbf{r}_{6,\mathbf{C}} = \begin{bmatrix} 0 \\ 0 \\ 0 \\ 0 \\ 1 \\ 0 \\ 0 \end{bmatrix}, \mathbf{r}_{7,\mathbf{C}} = \begin{bmatrix} 0 \\ \rho_1 \\ \rho_2 \\ 0 \\ 0 \\ c \\ \rho c^2 \end{bmatrix}, \tag{A13}$$

and the left eigenvectors are

$$\mathbf{K}_{\mathbf{C}} = [\mathbf{k}_{i,\mathbf{C}}] = \begin{bmatrix} \mathbf{k}_{1,\mathbf{C}} \\ \mathbf{k}_{2,\mathbf{C}} \\ \mathbf{k}_{3,\mathbf{C}} \\ \mathbf{k}_{4,\mathbf{C}} \\ \mathbf{k}_{5,\mathbf{C}} \\ \mathbf{k}_{6,\mathbf{C}} \\ \mathbf{k}_{7,\mathbf{C}} \end{bmatrix} = \begin{bmatrix} 0 & 0 & 0 & 0 & 0 & 1/2c & -1/2\rho c^2 \\ 1 & 0 & 0 & 0 & 0 & 0 & 0 \\ 0 & 1 & 0 & 0 & 0 & 0 & -\rho_1/\rho c^2 \\ 0 & 0 & 1 & 0 & 0 & 0 & -\rho_2/\rho c^2 \\ 0 & 0 & 0 & 1 & 0 & 0 & 0 \\ 0 & 0 & 0 & 0 & 1 & 0 & 0 \\ 0 & 0 & 0 & 0 & 0 & 1/2c & 1/2\rho c^2 \end{bmatrix}. \tag{A14}$$

These linearly independent eigenvectors for each matrix confirm that the primitive form of the flow model (3) is hyperbolic and, therefore, amenable to numerical solution by a time marching scheme.

APPENDIX B: PROPAGATION TIME OF PRESSURE WAVES IN THE OCEAN BASIN

As aforementioned, the water depth is 1 m in the experiment. At 15 °C the speed of sound in pure water is 1465 m/s, so it takes an acoustic signal (pressure wave) about 1.37 ms to travel a distance of 2 m. For the case with impact velocity 5.5 m/s, the second small spike reaches its peak value at about $t = 0.60$ ms. For the case with impact velocity 7 m/s, the second small spike reaches its peak value at about $t = 0.51$ ms. For both cases, the rise time of the first peak is around 1 ms. Considering these factors, the time for the pressure wave from building up to being reflected back is 1.60 ms for the first case ($v = 5.5$ m/s) and 1.51 ms for the second case ($v = 7$ m/s). These two values are close to the theoretical time 1.37 ms. Therefore, it seems reasonable to deduce that the second small spike is due to the reflection of pressure wave from the bottom of the ocean basin.

APPENDIX C: MEASUREMENT ERROR AND NUMERICAL MESH CONVERGENCE

To understand the repeatability or the error of measurement, the experiments were repeated more than seven times totally in the ocean basin for each impact condition. Regarding pure water entry, for example, the box and whisker graph is used to indicate different groups of data collected from experiments in Figure 19, which shows the minimum, lower quartile, median, upper quartile, and maximum of the peak pressures measured on the impact plate. The repeatability of peak pressure measurement for $v = 5.5$ m/s is higher than that for $v = 7$ m/s.

A numerical convergence study of the pure water impact loadings on the plate is also carried out by successively refining the mesh in the vertical direction. The total number of mesh cells used in this study is $80 \times M \times 80$, in which M is the number of cells in the vertical direction. The computed loadings are illustrated in Figure 20, where (a) presents the results for impact velocity 5.5 m/s and (b) shows the results for 7 m/s. The black dots and red crosses are the computed absolute pressures at P1 (plate centre) and P2 (near plate edge). The green squares are the computed total force on the plate.

This article is copyrighted as indicated in the article. Reuse of AIP content is subject to the terms at: http://scitation.aip.org/termsconditions. Downloaded to IP: 149.170.118.205 On: Tue, 26 Jan 2016 09:29:20

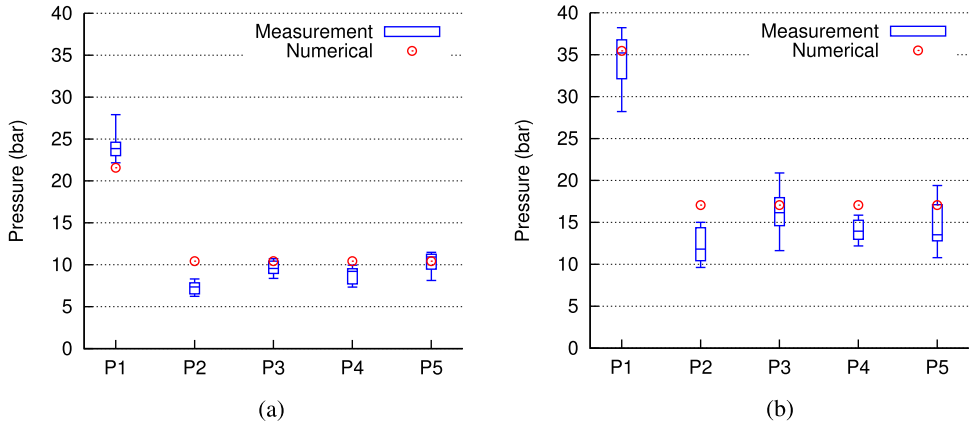

FIG. 19. Measured peak pressure loadings at five positions on the flat plate. The red circles are numerical computations on a fine mesh with $80\times1200\times80$ cells. (a) Impact velocity 5.5 m/s. (b) Impact velocity 7 m/s.

Figure 21 gives an example showing the measured and computed pressures at the centre of the 3D plate with impact velocity 7 m/s (pure water). The peak value calculated on the coarse mesh with $80 \times 600 \times 80$ cells is indeed lower than that of a fine mesh solution, but the impact loadings calculated on these two meshes agree in trend regarding the three principal stages of loading including the initial shock load, low-pressure fluid expansion load, and secondary reloading of the structure. These three stages have been repeatedly captured even on the coarser grids. The agreement in the trend of the impact loadings computed on different meshes demonstrates that our numerical model does not violate the physics to produce only one or two of the key stages. However, an incompressible multiphase flow code would eventually produce a physically inconsistent solution, which fails to predict the fluid expansion phase.

One computation of impact process with $80 \times 1200 \times 80$ mesh cells (in x–y–z direction) typically took about 14 days using the computing resource available to us. Doubling the mesh resolution in y direction will increase the computer time by a factor of four due to the doubling of number of mesh cells and the doubling of number of time steps. Therefore, computations using $80 \times 2400 \times 80$ (or even more) mesh cells would be considered impractical due to the excessive CPU time.

Considering this difficulty for 3D problems, we carried out a mesh convergence study for a 2D plate slamming problem in order to assess the consistency of our numerical scheme. The 2D flat plate has the same length (0.25 m), width (0.25 m), and thickness (0.012 m) as the 3D plate. The water

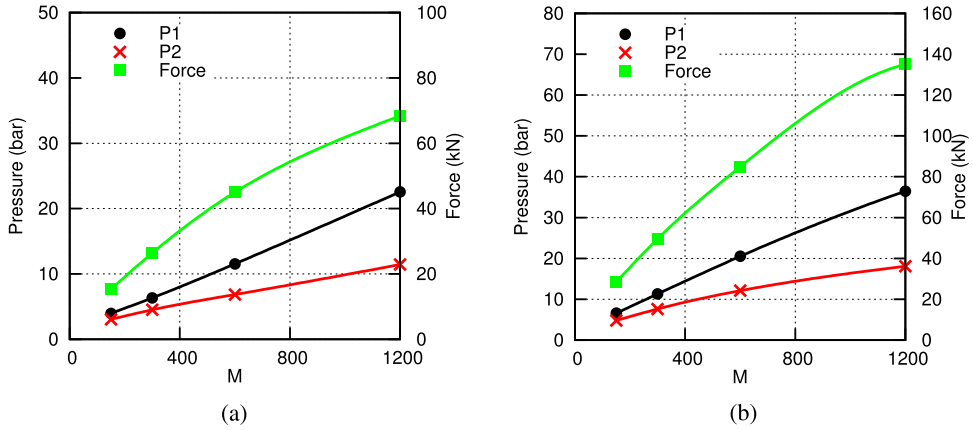

FIG. 20. Mesh convergence of the impact loadings on the 3D plate for pure water entry. The total number of mesh cells is $80\times M\times80$, in which M is the number of mesh cells in the vertical direction. (a) Impact velocity 5.5 m/s. (b) Impact velocity 7 m/s.

This article is copyrighted as indicated in the article. Reuse of AIP content is subject to the terms at: http://scitation.aip.org/termsconditions. Downloaded to IP: 149.170.118.205 On: Tue, 26 Jan 2016 09:29:20

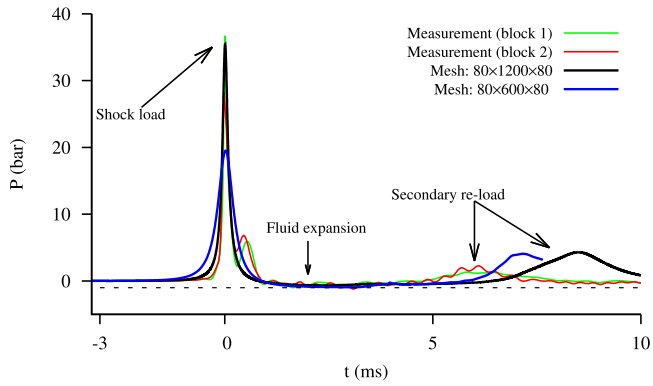

FIG. 21. Measured and computed pressures at the centre of the 3D flat plate for impact velocity 7 m/s (pure water). The coarse-mesh result also shows the principal three stages of impact loading including shock loading, low pressure loading, and secondary re-loading on the plate.

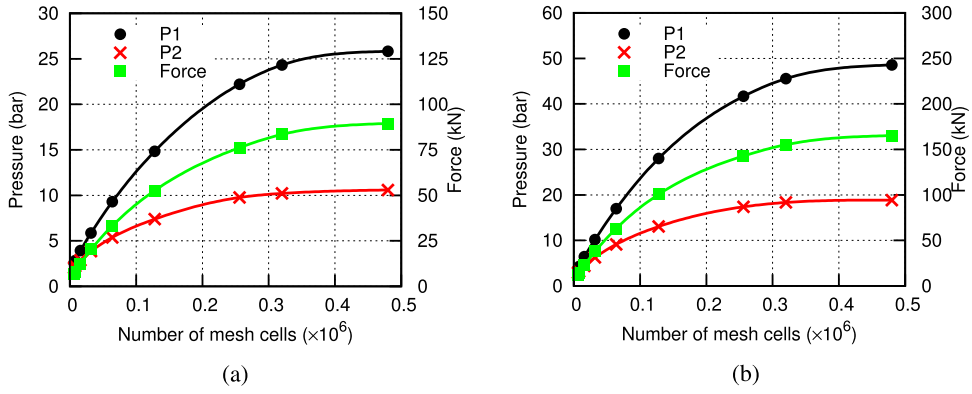

FIG. 22. A mesh convergence study of the peak impact loadings on a 2D flat plate for pure water entry. (a) v = 5.5 m/s. (b) v = 7 m/s.

entry velocity is either 5.5 m/s or 7 m/s (same as the 3D problem). In x direction, we fixed the number of mesh cells to 160, then we gradually refined the mesh in y direction from 40 up to 3000 cells. Figure 22 shows the variation of impact loadings on successively refined meshes. P1 and P2 represent the computed impact pressures at the plate centre and near the plate edge, respectively. The results illustrated in Figure 22 show mesh convergence of the impact loadings for the 2D problem, and this demonstrates the consistency of our numerical scheme with mesh discretisation.

One of our ongoing objectives is to improve the mesh convergence rate for water entry problems through the inclusion of anti-diffusion terms and the use of adaptive mesh refinement to improve the mesh resolution of free surface.

[1] J. Kay, "UK storms destroy railway line and leave thousands without power," BBC News, 2014, avilable at http://www.bbc.co.uk/news/uk-26042990.
[2] L. Rodgers and M. Bryson, "10 key moments of the UK winter storms," BBC News, 2014, avilable at http://www.bbc.co.uk/news/uk-26170904.
[3] O. Faltinsen, *Sea Loads on Ships and Offshore Structure* (Cambridge University Press, 1993).
[4] O. Faltinsen, "Hydroelastic slamming," J. Mar. Sci. Technol. **5**, 49–65 (2000).
[5] G. K. Kapsenberg, "Slamming of ships: Where are we now?," Philos. Trans. R. Soc., A **369**, 2892–2919 (2011).
[6] B. D. Rubin, "The basics of competitive diving and its injuries," Clin. Sports Med. **18**, 293–303 (1999).
[7] G.-d. Xu and W.-y. Duan, "Review of prediction techniques on hydrodynamic impact of ships," J. Mar. Sci. Appl. **8**, 204–210 (2009).
[8] K. Hughes, R. Vignjevic, J. Campbell, T. De Vuyst, N. Djordjevic, and L. Papagiannis, "From aerospace to offshore: Bridging the numerical simulation gaps–simulation advancements for fluid structure interaction problems," Int. J. Impact Eng. **61**, 48–63 (2013).
[9] E. Chan-Seng, F. Perrin, F. Segnarbieux, and N. Lonjon, "Cervical spine injuries from diving accident: A 10-year retrospective descriptive study on 64 patients," Orthop. Traumatol.: Surg. Res. **99**, 607–613 (2013).

This article is copyrighted as indicated in the article. Reuse of AIP content is subject to the terms at: http://scitation.aip.org/termsconditions. Downloaded to IP: 149.170.118.205 On: Tue, 26 Jan 2016 09:29:20

[10] D. Zhou, W. Wei, B. Tian, C. Wang, X. Shi, and X. Jiao, "Observation and management of retinal changes related to diving in professional divers," Chin. Med. J. (Engl. Ed.) **127**, 729–733 (2014).
[11] T. von Karman, "The impact on seaplane floats during landing," Technical Report No. NACA-TN-321, Aerodynamical Institute of the Technical High School, Aachen, 1929.
[12] W. Pabst, "Theorie des landestoß von seeflugzeugen," Z. Flugtech. Motorluftschiffahrt **21**, 217–226 (1930).
[13] H. Wagner, "Über stoß- und gleitvorgänge an der oberfläche von flüssigkeiten," Z. Angew. Math. Mech **12**, 193–215 (1932).
[14] A. A. Korobkin and V. V. Pukhnachov, "Initial stage of water impact," Annu. Rev. Fluid Mech. **20**, 159–185 (1988).
[15] S. D. Howison, J. R. Ockendon, and S. K. Wilson, "Incompressible water-entry problems at small deadrise angles," J. Fluid Mech. **222**, 215–230 (1991).
[16] W. K. Meyerhoff, "Added masses of thin rectangular plate calculated from potential theory," J. Ship Res. **14**, 100–111 (1970).
[17] Y. Fujita, "On the impulsive pressure of circular plate falling upon a water-surface (The 2nd report)," J. Zosen Kiokai **1954**, 105–110 (1954).
[18] J. Verhagen, "The impact of a flat plate on a water surface," J. Ship Res. **11**, 211–223 (1967).
[19] S.-L. Chuang, "Investigation of impact of rigid and elastic bodies with water," Technical Report No. NSRDC-3248, Department of the Navy, Washington, D. C., 1970, p. 20007.
[20] F. Huera-Huarte, D. Jeon, and M. Gharib, "Experimental investigation of water slamming loads on panels," Ocean Eng. **38**, 1347–1355 (2011).
[21] S. Okada and Y. Sumi, "On the water impact and elastic response of a flat plate at small impact angles," J. Mar. Sci. Technol. **5**, 31–39 (2000).
[22] M.-C. Lin and L.-D. Shieh, "Simultaneous measurements of water impact on a two-dimensional body," Fluid Dyn. Res. **19**, 125–148 (1997).
[23] N. Lange and T. Rung, "Impact tests in pure and aerated water," in *Proceedings of the ASME 2011 30th International Conference on Ocean, Offshore and Arctic Engineering* (ASME, Rotterdam, The Netherlands, 2011), pp. 1–9.
[24] P. D. Hicks, E. V. Ermanyuk, N. V. Gavrilov, and R. Purvis, "Air trapping at impact of a rigid sphere onto a liquid," J. Fluid Mech. **695**, 310–320 (2012).
[25] A. R. Crawford, "Measurement and analysis of wave loading on a full scale coastal structure," Ph.D. thesis, Plymouth University, Plymouth, UK, 1999.
[26] J. C. Scott, "The role of salt in whitecap persistence," Deep-Sea Res. Oceanogr. Abstr. **22**, 653–657 (1975).
[27] M. Walkden, A. Crawford, P. Bird, P. Hewson, and G. Bullock, "Wave impact loading on vertical structures," in *Proceeding ICE Coastal Structures and Breakwaters Conference* (Thomas Telford, London, 1995), pp. 273–286.
[28] H. Bredmose, D. Peregrine, and G. Bullock, "Violent breaking wave impacts. Part 2. Modelling the effect of air," J. Fluid Mech. **641**, 389–430 (2009).
[29] H. Bredmose, G. N. Bullock, and A. J. Hogg, "Violent breaking wave impacts. Part 3. Effects of scale and aeration," J. Fluid Mech. **765**, 82–113 (2015).
[30] A. B. Wood, *A Textbook of Sound* (G. Bell and Sons, London, 1941).
[31] T. Mai, D. Greaves, and A. Raby, "Aeration effects on impact: Drop test of a flat plate," in *Proceedings of the 24th International Ocean and Polar Engineering Conference* (International Society of Offshore and Polar Engineers, Busan, Korea, 2014), pp. 703–709.
[32] Z. H. Ma, D. M. Causon, L. Qian, C. G. Mingham, H. B. Gu, and P. M. Ferrer, "A compressible multiphase flow model for violent aerated wave impact problems," Proc. R. Soc. A **470**, 20140542 (2014).
[33] A. Kapila, R. Menikoff, J. Bdzil, S. Son, and D. Stewart, "Two-phase modeling of deflagration-to-detonation transition in granular materials: Reduced equations," Phys. Fluids **13**, 3002–3024 (2001).
[34] C. O. Ng and S. C. Kot, "Computations of a water impact on a two-dimensional flat-bottomed body with a volume-of-fluid method," Ocean Eng. **19**, 377–393 (1992).
[35] H. Mitsuyasu, "Shock pressure of breaking wave," in *Coastal Engineering Proceedings* (ASCE, 1966), Vol. 1, pp. 268–283.

This article is copyrighted as indicated in the article. Reuse of AIP content is subject to the terms at: http://scitation.aip.org/termsconditions. Downloaded to IP: 149.170.118.205 On: Tue, 26 Jan 2016 09:29:20